Investigating the Frequency and Inter-Annual Variability in Global Above-Cloud Aerosol Characteristics with CALIOP and OMI

Ricardo Alfaro-Contreras[1], Jianglong Zhang[1], James R. Campbell[2] and Jeffrey S. Reid[2]

[1]Department of Atmospheric Science, University of North Dakota, Grand Folks, ND

[2]Marine Meteorology Division, Naval Research Laboratory, Monterey, CA

Submitted to ACP

July

2015

Corresponding Author Contact: Dr. Jianglong Zhang, c/o Department of Atmospheric Sciences, 4149 University Avenue Stop 9006, University of North Dakota, Grand Forks, ND, USA

E-mail:jzhang@atmos.und.edu

ABSTRACT

Seven and a half years (June 2006-November 2013) of Cloud-Aerosol Lidar with Orthogonal Polarization (CALIOP) aerosol and cloud layer products are compared with collocated Ozone Monitoring Instrument (OMI) Aerosol Index (AI) data and Aqua Moderate Resolution Imaging Spectroradiometer (MODIS) cloud products, to investigate variability in estimates of bi-annual and monthly above-cloud aerosol (ACA) events globally. The active- (CALIOP) and passive-based (OMI-MODIS) techniques have their advantages and caveats for ACA detection, and thus both are used to derive a thorough and robust comparison of daytime cloudy-sky ACA distribution and climatology. For the first time, baseline above cloud aerosol optical depth (ACAOD) and AI thresholds are derived and examined (AI = 1.0, ACAOD = 0.015) for each sensor. Both OMI-MODIS and CALIOP-based daytime spatial distributions of ACA events show similar patterns during both study periods (December – May) and (June – November). Divergence exists in some regions, however, such as Southeast Asia during June through November, where daytime cloudy-sky ACA frequencies of up to 10% are found from CALIOP yet are non-existent from the OMI-based method. Conversely, annual cloudy-sky ACA frequencies of 20-30% are reported over Northern Africa from the OMI-based method, yet are largely undetected by the CALIOP-based method. Using a collocated OMI-MODIS-CALIOP dataset, our study suggests that the cloudy-sky ACA frequency differences between the OMI-MODIS- and CALIOP-based methods are mostly due to differences in cloud detection capability between MODIS and CALIOP as well as QA flags used. An increasing inter-annual-variability of ~0.3-0.4% per year (since 2009) in global monthly cloudy-sky ACA daytime frequency of occurrence is found using the OMI-MODIS based method. Yet, CALIOP-based global daytime ACA frequencies exhibit a near-zero inter-annual-variability. Further analysis suggests that the OMI derived inter-annual-variability of cloudy-sky ACA frequency may be affected by OMI row

anomalies in later years. A few regions are found to have increasing slopes in inter-annual variability of cloudy-sky ACA frequency, including the Middle-East and India. Regions with slightly negative slopes of the inter-annual variability of cloudy-sky ACA frequencies are found over South America and China, while remaining regions in the study show nearly zero change in ACA frequencies over time. The inter-annual variability of ACA frequency are not statistically significant on both global and regional scales, though, given relatively lacking sample sizes. A longer data record of ACA events is needed in order to establish significant trends of ACA frequency regionally and globally.

1. Introduction

The above-cloud aerosol (ACA) phenomenon, wherein significant active-based backscatter and passive-based scattered solar radiances are induced by particles above what are predominately lower tropospheric clouds, has gained an increased amount of attention from the scientific community (e.g. Haywood et al., 2004; Wilcox et al., 2009; Coddington et al., 2010; Devasthale and Thomas, 2011; Wilcox, 2012; Kacenelenbogen et al, 2014). In particular, whereas passive-based atmospheric retrievals are compromised by a binding inability to decouple aerosol, cloud and atmospheric radiances in the ACA scenario, corresponding cloud property retrievals are uniquely biased (Wilcox et al., 2009; Meyer et al., 2013; Alfaro-Contreras et al., 2014; Li et al., 2014). ACA further perturbs regional radiation budgets by absorbing and reflecting radiation from the cloud layers underneath the unidentified aerosol particle layer (e.g., Haywood et al., 2004), which again must be accounted for when estimating global cloud and aerosol forcing budgets and regional semi-direct impact on static stability and cloud feedback. Global oceans are covered with clouds nearly 70% of the time (e.g. Rossow and Schiffer, 1999), with almost non-existent corresponding ground-based verification data of ACA phenomena. This exacerbates the impact of ACA effects globally, limiting characterization of any quantitative impact and frequency of occurrence almost exclusively to satellite-based measurements.

ACA events are most effectively identified using active-based lidar measurements, which has been demonstrated using the Cloud-Aerosol Lidar with Orthogonal Polarization (CALIOP; Winker et al., 2010; Kacenelenbogen et al, 2014), one of the few such instruments presently in satellite orbit. CALIOP measures backscattered signals at the 532 and 1064 nm wavelengths, including segregated linearly-parallel and orthogonal polarization backscatter states in the former

channel. In particular, the active-profiling element is essential for decoupling aerosol and cloud scattering contributions in ACA events (Devasthale and Thomas, 2011). Utilizing four years of CALIOP Level 2 data (Winker et al., 2009), Devasthale and Thomas (2011) evaluated seasonal and latitudinal patterns of ACA for liquid water cloud events. Alfaro-Contreras et al. (2014) describe seasonal frequencies in ACA over the southern Atlantic Ocean off the West African coastline, as well as over the Gulf of Tonkin in Southeast Asia where high ACA loading episodes were found during the summer and fall months and early spring months, respectively.

Whereas limited process studies have helped raise awareness of the ACA problem overall, year to year variability in global ACA frequency distribution has not yet been developed with CALIOP. Despite a nearly eight-year (2006-present) CALIOP data archive available, one must be considerate of the fact that satellite lidar profiling is constrained presently to a single laser-illuminated curtain and roughly sixteen daily orbits of the planet. Questions thus arise about the representativeness of CALIOP datasets for some climatological analyses, like ACA, given its temporal persistence and spatial extent (Devasthale and Thomas, 2011; Yu et al., 2012). Additionally, for CALIPSO-based ACA studies to be meaningful, the potential impacts of signal deterioration to CALIOP derived aerosol optical depth (AOD) values need to be known. Despite the practical limitations of applying passive sensors for studying phenomena like ACA, then, the relatively wide field-of-view on passive imagers renders far greater data volume, which makes them more ideal options for a long-term study.

Ozone Monitoring Instrument (OMI) measurements have also been used for studying ACA events (e.g., Wilcox et al., 2009; Yu et al., 2012; Alfaro-Contreras et al., 2014). In particular, the OMI Aerosol Index (AI), computed using the difference between observed and calculated ultraviolet (UV) radiances (Torres et al., 2007), has been used to locate UV-absorbing

aerosols suspended over bright cloud decks (e.g. Yu et al., 2012, Torres et al., 2012). This technique, originally used on the Total Ozone Mapping Spectrometer (TOMS), can only be used to detect UV-absorbing aerosols, such as biomass burning smoke and desert dust aerosols and is sensitive to underneath cloud properties (e.g. Yu et al., 2012; Alfaro-Contreras et al., 2014). Further and compared with CALIOP, OMI measurements represent a relatively large surface footprint of 13x24 km at nadir, which limits cloud-clearing efficacies since footprints of this size are prone to sub-pixel cloud contamination (Torres et al., 2007). Collocated Moderate Resolution Imaging Spectroradiometer (MODIS) observations, however, as part of NASA's A-Train satellite constellation, which includes CALIOP (Stephens et al., 2002), can be utilized to distinguish and filter cloudy pixels/scenes within the OMI footprint.

Comparison of active vs. passive based sensors for evaluating the spatio-temporal coverage of ACA events, and for studying inter-annual variability of ACA occurrence on regional and global scales, represents a conservative means for conceptualizing the breadth of the problem. The goal of this work is, therefore, to compare and contrast distributions in global and regional ACA frequencies and their year-to-year variability using both CALIOP- and OMI-based approaches. Caveats to each approach are specifically identified, and thus qualified within the discussion so as to keep comparison as consistent and robust as possible. We highlight regions particularly susceptible to ACA occurrence, establishing a baseline for future ACA-induced biases in satellite cloud property retrievals overall.

2. Datasets and Methodology

CALIOP Level 2 5-km cloud and aerosol layer products (Winker et al., 2010) and OMI Level 2 Collection 3 UV aerosol products (OMAERUV; Torres et al., 2007) are paired with Collection 5.1 Aqua MODIS cloud products (MYD06_L2; King et al., 1997) from June 2006

through November 2013. Aerosol Robotic Network (AERONET; Holben et al., 1998) Level 2.0 Version 2 cloud-screened data are also used to assist the analysis.

For identification of ACA, 5-km CALIOP 532 nm cloud and aerosol layer products are used (Winker et al., 2009, 2010) for resolving aerosol extinction above apparent cloud top heights in each respective product file (e.g. Yu et al., 2012; Alfaro-Contreras et al., 2014). The 532 nm above cloud aerosol optical depth (ACAOD) is then solved by integrating the extinction coefficient over those corresponding bins (Liu et al., 2013; Kacenelebogen et al., 2014). The CALIOP-based inter-annual variability analysis may be affected by CALIOP signal deterioration over time. Thus, collocated AERONET datasets are used, as first order approximation, for evaluating instrument-related variation in the year-to-year variability of CALIOP AOD. Reported at eight spectral bands ranging from 0.34 μm – 1.64 μm (Holben et al., 1998), AERONET AOD datasets are frequently used for validating satellite retrievals (e.g., Zhang et al., 2001; Yu et al., 2003; Kaufman et al. 2005; Remer et al., 2005; Hahn et al., 2010; Shi et al. 2011; Sayer et al. 2012), as well as model simulated aerosol optical properties (e.g. Zhang et al., 2011; 2014).

The Level 2.0 cloud-screened and quality-assured AERONET AOD data (Eck et al., 1999) from all available coastal and island AERONET sites are used for collocating CALIOP data. AERONET AOD data are interpolated, based on a method described in Zhang and Reid (2006), to the 0.532 μm CALIOP wavelength and are spatio-temporally-collocated with CALIOP AOD data. Year-to-year changes in AOD retrieved from the CALIOP instrument are investigated by calculating the global monthly-mean AERONET and CALIOP AODs and comparing the two monthly aerosol loading averages. CALIOP observations found to be within 0.3 degrees latitude/longitude and ±30 minutes of corresponding AERONET observations are

considered collocated in space and time (see Omar et al., 2013 for a summary of the limitations pairing CALIOP and AERONET observations). In addition, we have used only pairs that have collocated AERONET AOD (0.532 μm) data less than 0.2 to exclude major aerosol episodes of continental origin. One additional quality assurance step is applied to exclude pairs with CALIOP AOD of larger than 0.6 for removing potentially noisy CALIOP data. In the case where several CALIOP observations are paired up with a single AERONET retrieval, a one-to-one relationship is established with the closest CALIOP observation.

OMI AI are used to isolate ACA events in those data. OMI AI and MODIS cloud datasets are spatio-temporally-collocated, given their position in the NASA "A-Train" constellation (e.g. Stephens et al., 2002), by collocating the two products with respect to overpass times and then identifying all temporally-collocated cloudy MODIS pixels located within the boundaries of the OMI footprint. Such methods are described further in Alfaro-Contreras et al. (2014). Cloud fractions from the Collection 5.1 MODIS MYD06 product, which are used to determine the opaqueness of the MODIS scenes, are reported at a 5 km horizontal resolution, are then leveraged for sub-pixel cloud clearing of the OMI AI. The MODIS cloud fraction is computed from the percentage of cloudy 1-km cloud mask product (MOD35) pixels within a given 5-km scene (e.g., Ackerman et al., 1998). It should be noted that this MODIS cloud fraction is reported regardless of the success of cloud optical property retrievals (e.g., cloud optical depth and Liquid Water Path). The, OMI and MODIS data are each filtered and quality-assured (described in detail in Alfaro-Contreras et al., 2014) to calculate respective global ACA distributions. The OMI and MODIS data are spatially and temporally collocated, and the collocated OMI AIs are assigned to 100% cloudy MODIS scenes (as determined by MODIS, with a COD > 0). This collocation process and methods are further described in Alfaro-

Contreras et al. (2014). However, cloud inhomogeneity is not considered, and we leave the topic for another study.

If multi-layer clouds exist, MODIS can only resolve the highest cloud layer most of the time. Thus, we focus on the highest level clouds in any given atmospheric column using CALIOP cloud layer products for a more accurate representation between the two techniques. The CALIOP data are filtered based on the study by Yu et al. (2012), where aerosol layers found with 'medium' or 'high' confidence are used. Note that, initially, cloudy scenes are defined as CALIOP COD > 0 for the CALIOP-based method and no QA steps are applied to the CALIOP cloud layer products to ensure the detection of all possible ACA events. The effect of QA flags from the CALIOP cloud layer products to the detected CALIOP ACA frequency is further explored in Section 4.2 (as well as shown in Devasthale and Thomas, 2011). It is known that that the OMI instrument has experienced row anomalies since 2008-2009 (http://www.knmi.nl/omi/research/product/, accessed on 22 Dec. 2014). Thus, the impact of the row anomalies on the inter-annual variability of ACA occurrence derived from OMI AI is explored later in this paper.

3. Above-Cloud Aerosol Baselines and Limitations

There are always aerosol particles above clouds (a fact that quickly becomes lost when discussing the basic physics of ACA relative to satellite observation). Therefore, there exists some baseline thresholds by which active backscatter and/or passive radiances become significant relative to a given physical process or retrieval (i.e., radiative forcing, heating rates, transmission estimates, cloud microphysical retrievals, etc.). Accordingly, each of the instruments subject to the ACA phenomenon in this study exhibit fundamental sensitivities to ACA detection, which impact our ability to characterize the problem fully. Therefore, the

196 baseline thresholds for significant ACA events need to be identified for both OMI- and CALIOP-
197 based ACA studies.

198 To conceptualize the problem, we look at the globally averaged cloud-top height for
199 clouds located under aerosol plumes, which is found to be roughly 2.0 km and compares well
200 with previous studies (Devasthale and Thomas, 2011). Thus, we consider the unique AERONET
201 site at Mauna Loa, Hawaii (LAT/LON, 3397 m above mean sea level). This free-tropospheric
202 ground site rests at an altitude roughly within the global mean cloud top heights. Indeed, this
203 physical feature of the site (that is, most commonly being above a cloud deck below) is one of
204 the key reasons for the importance of the site globally. The yearly mean Level 2.0 AERONET
205 AOD (500 nm) there ranges from 0.013-0.023 (500 nm) from 1996-2013, and provides a
206 generalized estimate for potential baseline ACAOD value globally. Kacenelenbogen et al.
207 (2014) report that the CALIOP lidar exhibits limitations in detecting ACA plumes with ACAOD
208 less than 0.02. This lower value may, therefore, represent an effective noise floor, whereby
209 CALIOP algorithm response below it is compromised.

210 Based on Kacenelenbogen et al. (2014), combined with the AOD climatology from the
211 Mauna Loa AERONET site analyses, we arbitrarily set the baseline CALIOP ACAOD value to
212 0.015. Still, the CALIOP ACAOD baseline of 0.015 is arbitrary. We thus investigate CALIOP-
213 based ACA frequency distributions by varying the baseline values to 0, 0.01, 0.015 and 0.02 as
214 shown in Fig. 1. Figures 1a-d show the cloudy-sky global ACA frequency distribution from
215 CALIOP, defined in Table 1, for the Dec.- May period, for baseline ACAODs of 0 (1a), 0.01
216 (1b), 0.015 (1c) and 0.02 (1d) respectively, using the CALIOP aerosol layer datasets. Note that
217 different from the cloudy-sky frequency, another way of measuring ACA frequency has been
218 proposed by Devasthale and Thomas (2011) and is referred as the all-sky frequency from

CALIOP in this study, also defined in Table 1. The difference between the two techniques is discussed in more detail during the section analyzing the year to year variation in ACA frequency occurrence.

Shown in Fig. 1, no clear difference is observed in the cloudy-sky ACA frequency by applying various CALIOP ACAOD baselines. A similar conclusion can also be made for the June- Nov period (Figs. 1e-1h). Thus, for the purposes of this paper, the baseline CALIOP ACAOD value of 0.015 (0.532 μm) is chosen, and the sensitivity of ACA inter-annual variability to the selection of the baseline CALIOP ACAOD is explored in a later section. Additionally, our selection of CALIOP ACAOD baseline has little effect on the background cloudy-sky ACA frequency, which is for the most part less than 5 % (dark blue) globally. Thus, we arbitrarily select 5% as the threshold between background and significant cloudy-sky ACA frequencies. For the remainder of the paper, ACA frequencies less than five percent are not considered for global distributions of ACA frequencies (except for sensitivity and case studies).

To derive the corresponding noise floor value for above-cloud OMI AI, a pairwise comparison of collocated above-cloud OMI AI and CALIOP AOD has been performed using one year (2007) of collocated OMI-MODIS and CALIOP data, as described in Alfaro-Contreras et al. (2014), though without any limitations on the cloud-top height. Figure 2a depicts the relationship between binned above-cloud OMI AI and CALIOP AOD segregated into six different underlying MODIS-derived CODs (Yu et al., 2012, Torres et al., 2012). The bin-averaged CALIOP ACAOD of 0.015, which reflects the baseline CALIOP ACAOD value chosen above, corresponds with OMI AI values of 0.7 - 1.2 for underlying MODIS CODs ranging from 0 to 20. Note that, if CALIOP ACAODs are biased low, the corresponding OMI AI thresholds may bias high using methods as shown in Fig. 2a.

Still, as suggested from Fig. 2a, baseline values of OMI AI vary from 0.7 to 1.2 depending on the underlying cloud properties. To further explore the issue, detected ACA events are evaluated using different baseline OMI AI values, similar to the CALIOP ACAOD baseline analysis and shown in Figs. 2b-2i, though using only those bin averages with cloudy-sky ACA frequency greater than five percent. Figures 2b-2e depict the multi-year (2006-2013) cloudy-sky ACA frequency global average for the Dec.-May period, by applying AI baseline thresholds of 0.7 (2b), 0.8 (2c), 0.9 (2d) and 1.0 (2e) respectively. With the use of the baseline OMI AI value of 0.7, most of the remote southern oceans stand out for significant case numbers. By increasing the AI baseline value to 1.0, in contrast, detected ACA events are significantly reduced. A similar conclusion can also be drawn from the June-Nov. period (Figs. 2f-i). Given that hand-held ship borne sun photometer measurements collected by the Marine Aerosol Network (MAN; Smirnov et al., 2011) show an averaged AOD (0.55 μm) of 0.07 or less from 30° to 60° S (Toth et al., 2013), significant ACA events are not likely over remote southern oceans. Thus, based on Figs. 1 and 2, CALIOP ACAOD of 0.015 and an above-cloud OMI AI of 1.0 are chosen as baselines. As we have now defined our baseline thresholds for ACA from both OMI and CALIOP, this enables us to create definitions of the various ACA frequencies used throughout this study, which are shown with further detail in Table. 1.

Selection of baseline CALIOP ACAOD and OMI AI is clearly subjective, and done for qualitative analysis in subsequent sections. There are multiple caveats that must be considered before constraining these values more accurately and representatively. First, as mentioned earlier, the CALIOP instrument has issues in detecting distinct optically-thin aerosol layers, especially during daytime. Additionally, it has been reported that CALIOP has a decreased sensitivity to stratospheric aerosols layers (Thomason et al., 2007; Winker et al., 2009). Third,

besides aerosol loading, OMI AI is also sensitive to parameters such as aerosol vertical distribution, optical depth of underlying cloud and aerosol single scattering albedo (e.g. Yu et al., 2012). Thus, setting a seasonal and regional based baseline for ACA requires a more in depth analysis and should be considered in future studies. Still, this study presents the first ever attempt to solve ACA baselines, and the thresholds selected are the best noise floors we can derive with the given inputs.

4. Comparison of ACA Global Climatology using Two Separate Techniques

4.1 ACA Global Climatology from all available MODIS, OMI and CALIOP data

Figure 3a depicts the multi-year gridded mean near-global distribution (180°W - 180°E, 45°S - 60°N) of the OMI-derived daytime cloudy-sky ACA frequency (defined in Table 1.) for December to May. Figures 3b and 3c show corresponding cloudy-sky daytime and nighttime frequencies, respectively, using CALIOP data (defined in Table.1). Figures 3d-3f show the corresponding information to Figs. 3a-3c for June to November.

Comparison of daytime cloudy-sky ACA frequency distribution is consistent between the two sensors and seasonal periods investigated, and depicted in Figs. 3g-3j. Some differences are distinct during December-May, as cloudy-sky ACA frequencies as high as 10 % are visible over the Gulf of Mexico from CALIOP, for instance, whereas they are non-existent from OMI-MODIS (Fig. 3a). Cloudy-sky ACA frequencies of 20-30 % are found with OMI-MODIS over high-latitude northern Asia, in contrast with CALIOP that shows no such activity (Fig. 3i). During June-November, both methods resolve ACA events over the west coast of Africa, as well as over the Middle East, of similar magnitude (10-60%). However, distinct differences can be found between the two datasets. Higher cloudy-sky ACA frequency values of 10-30% are found over North Africa using OMI-MODIS, in contrast with much lower values of 10-20% found

using CALIOP, for example. An OMI-based ACA study should correspond with a higher noise floor compared with that of an active sensor, based on OMI's much coarser spatial and vertical resolutions, an inability to resolve non-UV absorbing aerosols, and the fundamental decoupling of column-integrated radiances themselves. Still, if the OMI AI baseline is biased, it may introduce an additional difference between OMI-MODIS- and CALIOP-based ACA frequencies.

Cloudy-sky ACA frequencies as high as 10-30 % are found over North Africa for both periods from OMI-MODIS while CALIOP returns much lower percentages (10-20%) over the same region. This region is dominated by dust particle transport (Kaufman et al. 2005), which is detected by both OMI and CALIOP. Therefore, we suspect that their relative differences as derived in Figs. 3i and 3j are likely linked to the misidentification of thick dust plumes as clouds by the MODIS cloud-masking scheme over bright desert surfaces (e.g., Levy et al., 2013). Such a misclassification is also illustrated in a case study (July 8, 2007, over the Saharan region) as shown in Fig. 4. Over a section of CALIOP detected cloud free aerosol polluted regions (15-30°N, 2-6°W), where OMI AI values are above 2, cloud fraction of a unit (fully cloud cover) is reported by the MODIS MYD06 product, indicating a potential misclassification of aerosol plumes as clouds in the MODIS MYD06 product. Further differences observed between the two datasets may also be due to different algorithmic sensitivities exhibited relative to both the optical depth of the underlying cloud and overlying aerosol plume, the OMI AI and CALIOP AOD noise floors used to define the ACA events, the particular QA settings applied to any of our datasets, differences in cloud-detection techniques between CALIOP and MODIS or the inability of OMI to detect all aerosol types. We have further explored this issue in section 4.2.

Compared with daytime, increases in both the spatial extent and cloudy-sky CALIOP ACA frequencies are observable at night, as seen from Figs. 3b, c, e and f, over most regions.

Over the most common ACA regions, nighttime cloudy-sky ACA frequencies can be 10-30 % higher than during day, which may partially due to the stronger sensitivity of CALIOP at night allowing for detection of optically thin aerosol plumes. In particular, ACA events are observed with extended frequency over the west coast of North America year round and over the west coast of South America for the June-Nov. period. Cloudy-sky ACA frequencies at night, over both of these regions, are composed of optically-thin aerosol loading cases above our defined noise floor. Nighttime ACA events are also observed over the east coast of Asia year round. One reason for differences in spatial coverage between daytime and nighttime ACA events is plausibly linked to a lower planetary boundary layer that affects the formation of low clouds (e.g., Schrage et al., 2012). Still, the discrepancy between nighttime and daytime ACA events can be partially attributed to the potential detection of relatively diffuse ACA plumes that are more detectable during nighttime compared with day as a result of the higher signal to noise ratio for CALIOP nighttime data (e.g. Kacenelenbogen et al., 2014).

Shown in Fig. 5 are averaged above-cloud OMI AI and CALIOP AOD values for corresponding ACA events from Fig. 3. Figure 5a depicts the mean near-global distribution of OMI AI over MODIS-resolved cloudy skies, defined as OMI-MODIS collocated cloudy pixels (cloud fraction of unity) and OMI AI averaged for each 1° x 1° grid box, during December to May. Only bins with averaged AI greater than 1.0 are plotted in accordance with our defined noise floor. Also for December-May, Fig. 5b depicts multi-year mean gridded daytime CALIOP ACAOD averaged for each 2.5° x 2.5° grid box for CALIOP-defined cloudy pixels (COD > 0), using only bin averaged ACAOD greater than 0.015. Figure 5c features the same information as Fig. 5b, now for nighttime CALIOP retrievals.

334 During the Dec.-May period, elevated OMI AI values are observed over the Saharan
335 desert region of northern Africa, as well as in Southeast Asia off the coast of northern Vietnam.
336 In comparison with OMI AI, CALIOP AOD shows a much broader distribution of AODs greater
337 than the baseline (ACAOD > 0.015) for the entire globe. Bin averaged AIs greater than the
338 baseline (AI > 1.0) are sparse during the winter and spring months. Additionally, optically thin
339 aerosol plumes are observed over the Northern Pacific Ocean during the CALIOP nighttime
340 analysis (Fig. 5c), when compared to the daytime (Fig. 5b).

341 Figures 5d-5f depict the same information as Figs. 5a-5c, now for the Jun.-Nov. period.
342 This period exhibits a relatively large overall distribution of ACA events. In addition to the
343 Saharan dust outbreaks, elevated AI and AOD values over the southern Africa smoke region are
344 also found from both OMI and CALIOP datasets, respectively. This period exhibits large
345 aerosol loading and ACA frequency over Southern Africa and the southeast Atlantic Ocean.
346 High values of ACAOD are also found over the Indian Ocean and Arabian Sea, due likely to the
347 transport of dust aerosols from the east Saharan and Arabian Gulf regions (Satheesh et al., 2006).
348 Comparing Figs. 3 and 5 over regions such as the west coast of South and North America, it is
349 clear that cloudy-sky ACA frequencies are mostly attributable to relatively low aerosol loading
350 events. Figure 5 shows a drastically reduced distribution of averaged OMI AIs above the AI
351 baseline (1.0) in comparison to averaged CALIOP ACAODs above the AOD baseline (0.015).

352 Again, differences are visible here between day and nighttime CALIOP AOD
353 distributions. Off the Southwest coast of Africa, the development of marine stratus-type clouds,
354 as suggested from Fig. 6, may lead to higher ACAOD values at night. Over India and the
355 Middle East, we suspect that higher daytime ACAOD values may exist. Still, lower CALIOP

356 signal-to-noise during daytime may be a limiting factor that contributes significantly to the
357 difference.

358 It is likely that most ACA events occur over low-level liquid-phase cloud decks.
359 Therefore, spatial distributions of CALIOP-derived low-level clouds are investigated. Figure 6a
360 (6b) depicts the daytime (nighttime) multi-year mean distribution of low-level clouds (defined as
361 the ratio of CALIOP scenes with a COD > 0 and cloud-top height < 3km over total number of
362 CALIOP scenes) during December – May, for years 2006 to 2013. CALIOP cloud layer data are
363 gridded into 2.5° x 2.5° bins. Figures 6c and 6d depict the same information as Figs. 6a and 6b,
364 now from June – Nov., for years 2006 to 2013. Figures 6e and 6f depict the ratio between
365 daytime and nighttime low-level cloud frequencies per bin for the Dec.-May period and June-
366 Nov. periods, respectively. The ratio is as high as 2.0 over the Northern and Southern Africa
367 regions during June-Nov., as well as over the Western US annually. Such a high ratio between
368 day and nighttime data leads to a nighttime frequency of 10-20 % low-level cloud coverage
369 increase over most regions compared with daytime observations, plausibly due to diurnal
370 boundary layer effects.

371 A significant percentage of CALIOP-derived low-level clouds are plausibly
372 stratocumulus clouds, which are frequently observed over the west coasts of major continents
373 (e.g. Wood et al., 2012). Qualitative comparison of Figs. 5 and 6 indicates reasonable
374 consistency between high frequencies of CALIOP-defined low-level cloud formation and ACA
375 loading. With the exception of the Saharan region, again due to the possible misclassification of
376 thick aerosol plumes as clouds by MODIS discussed earlier, most ACA loading cases are found
377 where the CALIOP-defined low-level cloud formation six month frequency exceeds 20 %. This
378 indirectly confirms that most ACA outbreaks occur over CALIOP-defined low-level clouds.

379 It is also useful to evaluate ACA frequency relative to mean clear-sky AOD. Figures 7a-7d
380 depict the multi-year mean clear-sky CALIOP AOD for the same temporal and spatial domains
381 as Figs 5b, c, e and f, respectively. As opposed to the cloud-sky ACA aerosol loading (Fig. 5),
382 AOD loading over clear-skies shows more activity inland, as the formation of low-level clouds is
383 more common over coastal regions (ICCP, 2007). An inter-comparison among Figs. 5, 6 and 7
384 suggests that ACA events do not necessarily follow clear sky AOD patterns but rather those
385 above-cloud aerosol-polluted regions with a high frequency of low-cloud presence.
386
387 **4.2 ACA Global Climatology from the collocated MODIS, OMI and CALIOP dataset**
388 As illustrated in Fig. 3 for the Dec.-May daytime period, ACA events over North Africa
389 as derived from the OMI-MODIS–based method are not found from the CALIOP-based method.
390 Also, ACA events over India, as reported from the CALIOP-based method, are not visible from
391 the OMI-MODIS-based method. Similarly, for the June-November period, ACA events over
392 North Africa reported from the CALIOP-based method are not as frequent as those seen from the
393 OMI-MODIS-based method. Yet the ACA events detected from the CALIOP-based method
394 over Southern China are not visible from the OMI-MODIS-based method.
395 To identify differences between the OMI-MODIS- and CALIOP-based cloudy-sky ACA
396 global climatology, a collocated dataset has been constructed that includes spatially and
397 temporally-collocated MODIS, OMI and CALIOP data for the period of June 2006 – November
398 2008. Note that no collocated data are available after Nov. 2008 due to the row anomaly of the
399 OMI instrument. All three sensors are on board the A-train constellation, making temporal
400 collocation less of an issue, and we require the observational times of the three datasets to be
401 within +/- 30 minutes to be considered. To spatially collocate the three datasets, only MODIS

(OMI) observations within 0.04 degrees (0.2 degrees) of the center of a CALIOP data point (from the 5-km CALIOP aerosol and cloud layer products) are used. Using the collocated OMI-MODIS-CALIOP data set, differences in cloudy-sky OMI-MODIS- and CALIOP-based ACA frequencies are studied as functions of CALIOP cloud and aerosol QA flags (Devastahale and Thomas, 2011), the differences between MODIS and CALIOP reported cloud coverages, and aerosol properties (UV-absorbing versus non UV-absorbing aerosols).

Similar to Figs. 3a and b, Figs. 8a and d show the cloudy-sky ACA frequency as detected by the CALIOP- and OMI-MODIS-based methods respectively, but with use the OMI-MODIS-CALIOP collocated dataset, for the Dec.-May period. Figures 8b (8e) and 8c (8f) show the all-sky ACA frequency and cloudy sky frequency for the CALIOP- (OMI-MODIS-) based methods. As mentioned in Table 1, all-sky ACA frequency is defined as the number of ACA events divided by all data points. Thus, Figs 8b (8e) and 8c (8f) can also be considered as ACA event data counts and cloudy-sky data counts for the CALIOP- (OMI-MODIS-) based method. Readers should be aware that the spatial distribution of MODIS cloud fraction, as shown in Figs. 8f and l, differ from the spatial distribution of cloud fraction obtained from the standard MODIS cloud products (e.g. King et al., 2013) for a few reasons. First, Figs. 8f and 8l are constructed using the MODIS cloud fraction values from a collocated OMI, CALIOP and MODIS dataset, and thus, only near-nadir MODIS cloud mask data are used. Also, cloud fraction values (at a 5 km resolution) from the MODIS MYD06 product are used. To be consistent with the OMI-MODIS analysis, only the 5-km granules that are 100% cloudy (or 25 1-km MODIS pixels within a 5-km granule are all cloudy) are counted as cloudy granules. Thus, broken and/or non-contiguous clouds may be excluded in the cloud fraction calculation.

The first thing to notice from these data is that cloudy sky frequency from the CALIOP-based method is higher than that of the OMI-MODIS-based method. The differences in cloudy sky frequencies are not unexpected, as the CALIOP-based method can detect optically-thin clouds (such as thin cirrus clouds) for which the OMI-MODIS-based method is limited (e.g., Toth et al., 2013). Also, the all-sky ACA frequencies from CALIOP- and OMI-MODIS-based methods show similar magnitudes for both the Dec.-May and June-Nov. periods. Thus, the higher cloud-sky ACA events over North Africa, as reported from the OMI-MODIS-based methods, are likely due to the differences in cloud detection capability among the different sensors.

For the Dec.-May period, higher all-sky ACA frequency is reported from the CALIOP-based method over India. A similar situation is also found for the June-Nov. period over Southeast Asia. While one would suspect that the greater number of ACA events over India and Southeast Asia regions could be due to the fact that the OMI-MODIS based method is only sensitive to non UV-absorbing aerosols, we also evaluated the issue with respect to CALIOP QA flags. Figure 9 shows global plots of cloudy sky frequency and all-sky ACA frequencies from the original QA metrics used to generate Fig. 3, as well as global plots altering CALIOP aerosol and cloud QA flags to 'lenient', 'intermediate' and 'strict'. Here, the CAD scores and Feature Classification Flags are used to define the quality of each retrieval. In order for a feature to be considered lenient, intermediate or stringent quality, its CAD score absolute value must be greater than either 0, 20 and 70, respectively. In addition, the feature flag must also return at least 'low', 'medium' and 'confident' result for the 'lenient', 'intermediate' and 'stringent' QA levels, respectively as defined in Liu et al. (2009).

Figures 9a-9c show the distributions of cloudy sky frequency with the use of lenient, intermediate and strict CALIOP cloud QAs, respectively. These data reflect how cloud QA exhibits only a minor effect on the spatial distribution of cloudy sky frequencies. Figures 9d-9f show the spatial distribution of all-sky ACA frequency with the 'lenient' aerosol QA setting but with the cloud QA levels of 'lenient', 'intermediate' and 'strict', respectively. Clearly seen from Figs. 9d and 9e, with the changing of cloud QA setting from 'lenient' to 'intermediate', are that the CALIOP-based all-sky ACA frequencies are much reduced over North Africa, the Middle-East, India and Southern China. This indicates that a portion of the observed differences between the OMI-MODIS- and CALIOP-based methods may due to cloud QA. Similarly, when we hold the cloud QA setting constant at 'lenient' while varying the aerosol QA setting from 'lenient' to 'intermediate' and 'strict' (Figs. 9g-9i), no significant changes in all-sky ACA frequencies are found. We repeat the process for the June-November period, as shown in Figs. 9j-9r, and similar conclusions are found.

The CALIPSO Level 2 cloud and aerosol layer products include cloud retrievals conducted using horizontal averages at the three extended settings (e.g. 5, 20 or 80 km averages). While 5 km averaging detects the most "reliable" cloud and aerosol signals, the 80-km averaging locates features with "weaker" signals (Vaughan et al., 2009). Since the CALIPSO Level 2 cloud and aerosol layer products are used in this study, the results presented here shall include horizontal averages from the three setting as mentioned. In addition, using CALIOP's ability to distinguish different aerosol types, we find that absorbing aerosols (dust, smoke and polluted dust) constitute about 80 % of ACA particles over southeast Asia during June – Nov., and more than 90 % over India during the Dec. – May period. Thus, OMI's inability to detect all aerosol types may play a minor role in the observed ACA frequency differences over these regions. On

the contrary, the differences in cloud detection capability, the QA settings and their arbitrary thresholds used are instead likelier be the primary causes for the discrepancies between OMI-MODIS- and CALIOP-based methods. Still, aerosol type discrimination from CALIOP measurements has its own limitations, and we leave this topic for a future paper to explore.

5. Inter-Annual Variability of Global ACA Frequency

An analysis of the year-to-year variation in global cloud-sky ACA frequency is carried out for five different scenarios. The different scenarios are: OMI daytime cloudy-sky frequency, CALIOP daytime cloudy-sky and all-sky frequencies and CALIOP nighttime cloudy-sky and all-sky frequencies. As suggested from Section 4.2, only CALIOP data with both cloud and aerosol QA settings as either 'medium' or 'highest' confidence levels are used hereafter. Figure 10 shows CALIOP daytime cloudy-sky frequency (red) and all-sky frequency (blue), CALIOP nighttime cloudy-sky frequency (orange) and all-sky frequency (purple), and OMI daytime cloudy sky-frequency (green). Each data point represents the global monthly-mean ACA frequency of CALIOP and OMI calculated from 2.5° and 1° gridded ACA frequencies, respectively.

An increase in the OMI cloudy-sky ACA frequency over the study period is apparent in this global dataset, most noticeably since 2009. However, this inter-annual variability is not matched in the CALIOP data. The seasonal variation in ACA frequency is observed from year-to-year for both OMI and CALIOP (dashed lines). However, from the year-to-year variation lines (showing a percentage change per year), only the OMI daytime cloudy-sky frequency shows a significant increase over this time period (solid lines). The increasing inter-annual variability in OMI derived daytime global cloudy-sky ACA frequency, which is not apparent in

any of the CALIOP derived global cloudy-sky ACA frequencies, is troublesome and may be attributed to any of the different sensitivities of the two techniques, including cloud and aerosol optical properties, aerosol-cloud separation distance, and/or deficiencies in the OMI data products. As will be described below, we further investigate several aspects of the observed increasing in inter-annual variability in the OMI derived daytime cloudy-sky global ACA frequency.

Given the unexpected monotonic increase in global ACA frequency derived using OMI AI data over the course of our study, we examine the inter-annual variability in the OMI daytime cloudy-sky ACA frequency more closely. Figure 10 indicates a near-zero increase in the seasonal averages during the first few years of the study, with frequencies increasing at a rate of roughly 0.3-0.4% per year starting in 2009. This time period coincides with the start of OMI data loss due to row anomalies, as mentioned above, leading us to further investigate this as a possible reason for the increase in the observed OMI cloudy-sky ACA frequency. Note that we detected data loss while collocating OMI and CALIOP datasets and found no collocated pixels after 2008; a possible sign that the data loss is likely affecting OMI nadir viewing pixels. This is illustrated in Fig. 11a, which depicts a single swath of OMI AI over the African continent on 1 August 2007 where only OMI pixels with valid AI are shown. The data loss affected a large portion of the OMI AI data near the nadir regions of each OMI AI swath, as shown from a swath in 1 June 2009 (Fig. 11b).

Given that the data loss affects mostly nadir-viewing OMI pixels, OMI AI are evaluated as a function of the OMI sensor's viewing zenith angle (VZA) shown in Fig. 12. All OMI AI pixels for one year (2007) are averaged into one-degree VZA bins. Averaged OMI AI values at the edge of the swath are generally higher by about one AI unit than retrievals taken near the

center of the swath. Thus, our analysis, which examines inter-annual variability in the OMI-derived ACA frequency, is compromised due to viewing geometry bias impacting later years of the OMI aerosol products. The remainder of the paper will focus solely on year to year variation derived from CALIOP ACA frequencies, and no further discussion of OMI AI frequencies will be carried out.

Next, AERONET AOD data are used to identify possible bias in the CALIOP lidar due to potential signal deterioration in the instrument. Figure 13 depicts the year-to-year variation in the clear-sky AOD derived using collocated CALIOP-AERONET data over all coastal and island AERONET stations (Zhang and Reid, 2006). The inter-annual variability in global AOD similar to those for the collocated AERONET and CALIOP data as shown in Fig. 13 seems to suggest that potential deterioration issue from CALIOP are rather insignificant to our ACA study.

6. Sensitivity Study

We next investigate the impact that our noise floor thresholds for overlying CALIOP AOD and/or underlying COD exhibit on derived global CALIOP cloudy-sky ACA frequency. All CALIOP cloud and aerosol layer datasets are reprocessed such that the following conditions are met: (a) the underlying COD is greater than 0.3 and 2.5, respectively, (b) the AOD of the above-cloud aerosol plume is greater than 0, and (c) both conditions (a) and (b) are true. Passive-based radiance retrievals have been shown to lack sensitivities to optically-thin cloud detection for optical depths less 0.3 (Sassen and Cho, 1992; Ackerman et al., 2008; Holz et al., 2008). Thus, restricting the CALIOP COD to this threshold offers a more direct comparison of CALIOP- and OMI-based ACA frequencies. However, given that this range of optical depth corresponds with relatively high cirrus clouds, for which little contribution to the overall sample is expected, and broken low-level liquid phase clouds that are biased to ambiguously low values

539 from signal aggregation effects in the 5-km product (Leahy et al., 2012; Campbell et al., 2015),
540 this higher threshold provides a more representative basis for evaluation. We re-compute the
541 monthly global mean cloudy-sky frequency for each of the CALIOP-constrained samples
542 defined above during both daytime and nighttime. The inter-annual variability in global cloudy-
543 sky ACA frequency derived from CALIOP are shown in Fig. 14. Corresponding sample sizes
544 and mean global frequencies are shown in Table 2.

545 In comparison with the unfiltered data from the daytime (solid red) and nighttime (dotted
546 red) analyses, the various threshold techniques, including the filtering of CALIOP ACAOD
547 according to our floor noise, correspond with significant variance in our results. However, all
548 sensitivity tests seem to show the same slightly-negative trend in cloudy-sky ACA frequency.
549 Although, those ACA events found over optically thicker clouds (COD > 2.5) seem to show
550 more of a null inter-annual variability over time rather than a slightly-negative inter-annual
551 variability in the CALIOP global ACA frequency. The COD threshold tests raises the daytime
552 mean global cloudy-sky frequency from 1.8% to 2.0 and 2.5% for the 0.3 and 2.5 COD
553 thresholds, respectively. This corresponds with a reduction in the sample size of approximately
554 0.4 (COD < 0.3) and 0.6 (COD < 2.5) million scenes when compared with the unfiltered
555 methods. During the nighttime analysis, the global mean cloudy-sky frequency is changed from
556 4.5% to 6.1 and 8.1%, respectively, while data counts change to 2.8 and 2.1 million globally for
557 the corresponding nighttime COD threshold tests. Setting a noise floor threshold on the AOD
558 reduces mean global cloudy-sky ACA frequencies by 0.33 and 1.9% for day and nighttime
559 analyses, respectively, corresponding with a reduction of global data counts of 0.3 and 1.6
560 million scenes. After screening out millions of samples during this sensitivity analysis, the same
561 near-zero or decreasing trend is found for CALIOP ACA frequencies, which is indication that

562 neither cloud or aerosol thresholds, or lack there-of, have a major impact on the inter-annual
563 variability of global CALIOP cloudy-sky ACA frequency.
564
565 **7. Regional Year-to-Year Variation Analysis**
566 A regional analysis of cloudy-sky ACA frequency is also conducted, consistent with
567 methods described above for global analysis. Regional analyses were chosen over high ACA
568 frequency regions, as indicated from Fig. 3. The nine regions of interest, shown in Table 3 and
569 indicated by the red boxes in Fig. 3, are: Northern Saharan Africa, Southern Africa, Southeast
570 Asia, China, the Middle East, South America, India, North America, and the Southern Oceans.
571 Figure 15 shows the regional cloudy-sky de-seasonalized ACA frequency for CALIOP daytime
572 (blue) and nighttime (teal) analyses, along with linear regression lines (described earlier for the
573 global analysis). Positive inter-annual variability in the cloudy-sky ACA frequency is found
574 over the Middle East and India for both daytime and nighttime. In contrast, decreasing inter-
575 annual variability in the cloudy-sky ACA frequency are found over China and South America for
576 both daytime and nighttime. All other regions correspond with a negligible change in cloudy-
577 sky ACA frequency during the study period.
578 A regional analysis of variation of cloud coverage over time is also conducted in order to
579 investigate whether the observed increases in ACA frequency over time are a result of cloud
580 coverage or aerosol loading. Positive AOD trends are observed from both regions (Zhang and
581 Reid, 2010; Hsu et al., 2012). Cloud cover frequency exhibits an insignificant trend over India
582 indicating that the ACA frequency increase may be due to aerosol loading increase over the
583 region. The observed increase in cloudy-sky ACA frequency over the Middle-East, however,
584 may be also due to the aerosols, as a slight decrease cloud coverage frequency is observed over
585 time over this region. Inter-annual variability and its significance are also calculated for each of

586 the regional and global analyses shown in Table 3 using methods described by Weatherhead et
587 al. (1998). As is apparent from Table 3, none of the trends are statistically significant (i.e., trend
588 significance > 2) with a confidence interval of 95%. Applying methods described in
589 Weatherhead et al., (1998), we determine that an ACA data record spanning 37 and 36 years is
590 needed to detect a 1 % yearly change with 95 % confidence, in cloudy-sky ACA frequency for
591 day and nighttime, respectively.

592 Inter-annual variability for both ACAOD and cloud-free AOD are also calculated
593 globally and for all regions shown in Table 3. Globally, the inter-annual variabilities of clear-sky
594 AOD and ACAAOD are slightly positive, while the ACA frequency is negative during both day
595 and night. Regions corresponding with a negative trend of all three parameters (ACA frequency,
596 ACAOD, and clear-sky AOD) include: Southeast Asia (nighttime) and South America
597 (nighttime). The Middle East (day and night) and India (day) regions exhibit positive trends for
598 all three parameters. The remaining regions exhibit a combination of positive, negative or near-
599 zero trends in all three parameters.

600

601 **8. Conclusions**

602 Using Cloud-Aerosol Lidar with Orthogonal Polarization (CALIOP) layer products and
603 collocated Ozone Monitoring Instrument (OMI) Aerosol products and Aqua Moderate
604 Resolution Imaging Spectroradiometer (MODIS) cloud products data from June 2006 –
605 December 2013, spatial distributions, including global and regional variabilities, of above cloud
606 aerosol (ACA) events are studied and compared. Active-based profiling is considered an optimal
607 means for identifying ACA occurrence. OMI identification is restricted to ultra-violet (UV)-
608 absorbing ACA events (i.e., smoke), in contrast, through the Aerosol Index (AI) parameter.
609 However, the relatively wide field-of-view of the paired OMI/MODIS datasets, in tandem,

provide greater data volume overall, which serves as a relatively well-characterized reference for comparing with CALIOP.

The primary findings of this study are:

1. Baseline values for passive-based OMI AI and active-based CALIOP above-cloud aerosol optical depth (ACAOD) are established in order to distinguish background noise from signal due to significant ACA events such as dust outbreaks and biomass burning. The "noise floor" for OMI AI and CALIOP are applied to their respective data sets during processing. However, caution should be exercised when using these baselines, as they are an approximation and will vary depending on ancillary observational parameters for OMI and day versus nighttime sensitivity for CALIOP.
2. Despite fundamental differences in spatial and vertical samplings, as well as sensitivity to ACA aerosol types, both OMI- and CALIOP-based techniques broadly resolve consistent global distributions of cloudy-sky ACA frequency. For example, both capture ACA events over the Northwest Coast of Africa and the Arabian Peninsula during the December-May period, and over the North- and South-west Coast, as well as the Southeast Coast of Africa, the Arabian Peninsula and Arabian Sea during the June - November period. Still, discrepancies, as expected, are present. For example, daytime cloudy-sky ACA frequencies of up to 10% are found from CALIOP over Southeast Asia during the June-Nov. period while such ACA events are none existent using OMI-based method. Over North Africa, cloudy-sky ACA frequencies of around 20-30% are reported for both periods from the OMI-based method, yet such events are largely undetected by

634 the CALIOP-based method. We suspect that heavy dust plumes may be
635 misidentified as clouds by the passive-based method, thus causing an unexpected
636 rise in the passive-based derived cloudy-sky ACA frequency over that region.
637 3. The differences between the OMI- and CALIOP-based daytime cloudy-sky ACA
638 frequencies are explored using a collocated OMI-MODIS-CALIOP dataset for the
639 period of June 2006 – November 2008. Our analysis shows that the difference in
640 cloud detectability between the MODIS and CALIOP instruments, as well as the
641 QA flags applied, are the major reasons for the differences. Although the OMI-
642 MODIS–based method is only sensitive to UV-absorbing aerosols and the
643 CALIOP-based method is capable of detecting ACA events of all aerosol types,
644 we did not find this to be one of the major reasons for the difference in ACA
645 frequencies.
646 4. CALIOP nighttime data exhibit slightly larger distributions and a 10-20 % greater
647 cloudy-sky ACA frequency annually in comparison with daytime. This may be
648 due the subsidence of the planetary boundary layer at night, influencing
649 frequencies of low-cloud formation, as well as the impact of higher signal-to-
650 noise in CALIOP datasets for subsequent Level 2 analysis partly controlled for in
651 our study by applying the noise floor. To the latter point, previous study has
652 shown relative stability between day/night CALIOP aerosol products (Campbell
653 et al., 2012). However, the implicit effect on the vertical distribution of aerosol
654 occurrence was not specifically investigated. More detailed study is needed to
655 reconcile this finding.

5. We find a near-zero negligible slope in the global CALIOP cloudy-sky and all-sky ACA frequencies. However, OMI-MODIS cloudy-sky daytime ACA frequencies show an increase of ~0.3-0.4 % / year since 2009, possibly due to a significant loss in the OMI data starting in 2009 mostly for nadir viewing pixels. Investigation of the relationship between OMI Aerosol Index (AI) and satellite viewing zenith angle, suggests a viewing angle dependency of OMI AI. Considering that OMI AI increases near the edge of the viewing swath, it is possible that the overall increase in ACA frequency is due to the significant loss of OMI AI data during later years of the study.
6. Changes in the cloudy-sky global ACA frequency and data counts ranging from 2-4 % and 1-3 million, respectively, are found as a result of applying a variety of thresholds to the ACAOD and/or underlying cloud optical depth (COD) during sensitivity analysis. COD thresholds of 0.3 and 2.5 filter high cirrus clouds and non-contiguous low-level water clouds, respectively. CALIOP data are further reprocessed with no restriction to the ACAOD. Most threshold tests show a reduction in global ACA frequencies however those ACA events located over optically thick clouds (COD > 2.5) show a near zero slope in the ACA frequency variability. However, a significant change over time to CALIOP global day or nighttime ACA frequency is not apparent.
7. Globally, clear-sky AOD and ACAOD temporal variations are slightly positive while cloudy-sky ACA frequency exhibits a slightly negative inter-annual variability in both the day and night times. Some select regions examined globally, selected for their relatively high ACA frequency overall, exhibit a

consistent inter-annual variability in all three parameters. For example, statistically significant increases in clear sky AOD are found over India and Middle-East from various passive based analysis (e.g. Zhang and Reid, 2010). Increasing in cloudy-sky ACA frequencies are also found for the two regions for the study period of 2006-2013. Other regions exhibit agreement between some, but not all, parameters. However, neither the regional or global trends of any of the three parameters are statistically significant. An ACA data record spanning at least 30 years is needed in order to report a 10% per decade change in ACA frequency with 95% confidence.

This study confirms that significant (i.e., resolvable with the techniques applied) ACA events occur with a frequency of 1-8% globally and as high as 30-50 %, regionally, over some of the most ACA-abundant regions. The two complementary techniques applied to locate ACA events and derive global and regional distributions and both exhibit strengths and weaknesses. This study shows that, when used simultaneously, combined passive/active analysis can help present a more comprehensive analysis of ACA than a single-sensor analysis alone. However, the analysis strongly reinforces the use of active-based lidar profiling for distinguishing aerosol presence that perturbs passive-based column-integrated radiative parameters. The vertical distribution and optical properties of aerosol and cloud layers are fundamental to accurate column radiative closure. The effects cloud-aerosol overlap can exhibit on cloud and aerosol property retrieval techniques demands some coordinated active/passive observation for ensuring clarity and limiting bias in top-of-atmosphere retrievals.

Due to the extensive spatial coverage and consistency of retrieved datasets from space-borne instruments, trend analyses, and the need for consistent multi-sensor profiling, should

become primary motivating factors behind mission design and life expectancy in orbit. Our analysis shows that in a few decades, proper analysis of ACA trends are possible through continuation of a CALIOP/OMI-like paradigm. Ultimately, this work, paired with Alfaro-Contreras (2014) and others, have broadly conceptualized the ACA problem globally. Past studies have shown that ACA events represent a fundamental climate phenomenon on a global scale (Peters et al. 2011), thus ACA requires specific long term monitoring. Trend analysis, then, will help ultimately distinguish this attribute, and thus whether or not ACA is simply noise or a radiatively-significant process that is sensitive to changes in land-use globally and a fluctuating frequency and distribution of elevated aerosol particles over time. Future satellite mission designs should emphasize extending the life of these instruments for application to environmental parameter inter-annual variability studies.

Acknowledgements

This research is funded through the support of the Office of Naval Research Codes 322. Author RAC is supported by the NASA project NNX14AJ13G. Author JRC acknowledges the support of the NASA Interagency Agreement IAARPO201422 on behalf of the CALIPSO Science Team. We thank the AERONET program and their contributing principal investigators for collecting and maintaining the sun-photometer data. CALIOP cloud and aerosol layer data were obtained from the Atmospheric Science Data Center. MODIS cloud data were obtained from the Goddard Space Flight Center Level 1 and atmospheric archive and distribution center system. The OMI aerosol data were obtained from the Goddard Earth Science Data Center and

Information Service Center. We thank Abhay Devasthale, Karsten Peters, Hiren Jethva and two other anonymous reviewers for their constructive comments and suggestions.

References

Ackerman, S.A., Strabala, K.I., Menzel, W.P., Frey, R.A, Moeller, C.C., and Gumley, L.E.: Discriminating clear sky from clouds with MODIS, *J.Geophys. Res.,103(D24),*32141-32157, doi:10.1029/1998JD200032, 1998.

Ackerman, S.A., Holz, R.E., Frey, R.E., Eloranta, R.W., Maddux, B., and McGill, M.J.: Cloud detection with MODIS: Part II. Validation, *J. Atmos. Oceanic Technol., 25,* 1073-1086.,2008.

Ackerman, S. A., Frey, R., Strabala, K., Liu, Y., Gumley, L., Baum, B., and Menzel, P.: Discriminating clear-sky from cloud with MODIS algorithm theoretical basis document (MOD35), ATBD Reference Number: ATBD-MOD-06, 2010.

Alfaro-Contreras, R., Zhang, J., Reid, J. S., Campbell, J. R., and Holz, R. E.: Evaluating the impact of aerosol particles above cloud on cloud optical depth retrievals from MODIS, J. Geophys.Res. Atmos., 119, 5410–5423, doi:10.1002/2013JD021270, 2014.

Brioude, J., Cooper, O. R., Feingold, G., Trainer, M., Freitas, S. R., Kowal, D., Ayers, J.K.,Prins, E., Minnis, P., McKeen, S. A., Frost, G. J., and Hsie, E.-Y.: Effect of biomass burning on marine stratocumulus clouds off the California coast, Atmos. Chem. Phys., 9, 8841–8856,doi:10.5194/acp-9-8841-2009, 2009.

Campbell, J. R., Tackett, J. L., Reid, J. S., Zhang, J., Curtis, C. A., Hyer, E. J., Sessions,W. R., Westphal, D. L., Prospero, J. M., Welton, E. J., Omar, A. H., Vaughan, M. A.,and Winker, D. M.: Evaluating nighttime CALIOP 0.532 μm aerosol optical depth and extinction coefficient retrievals, Atmos. Meas. Tech., 5, 2143–2160, doi:10.5194/amt-5-2143-2012,2012.

750 Campbell, J. R., Vaughan, M. A., Oo, M., Holz, R. E., Lewis, J. R., and Welton, E. J.:
751 Distinguishing cirrus cloud presence in autonomous lidar measurements, Atmos. Meas.
752 Tech., 8,435–449, doi:10.5194/amt-8-435-2015, 2015.
753 Chand, D., Anderson, T. L., Wood, R., Charlson, R. J., Hu, Y., Liu, Z., and Vaughan, M.:
754 Quantifying above-cloud aerosol using space borne lidar for improved understanding of
755 cloudy sky direct climate forcing, J. Geophys. Res., 113, D12306,
756 doi:10.1029/2007JD009443, 2008.
757 Chand, D., Wood, R., Anderson, T. L., Satheesh, S. K., and Charlson, R. J.: Satellite-derived
758 direct radiative effect of aerosols dependent on cloud cover, Nat. Geosci., 2, 181–
759 184,doi:10.1038/NGEO437, 2009.
760 Coddington, O. M., Plewskie, P., Redemann, J., Platnick, S., Russell, P. B., Schmidt, K. S.,
761 Gore, W. J., Livingston, J., Wind, G., and Vukicevic, T.: Examining the impact of
762 overlying aerosols on the retrieval of cloud optical properties from passive remote
763 sensing, J. Geophys.Res., 115, D10211, doi:10.1029/2009JD012829, 2010.
764 Devasthale, A. and Thomas, M.A.: A global survey of aerosol-liquid water cloud overlap based
765 on four years of CALIPSO-CALIOP data, Atmos. Chem. *Phys.*,*11*,1143-
766 1154,doi:10.519/acp-11-1143-2011, 2011.
767 Eck, T. F., Holben, B. N., Reid, J. S., Dubovik, O., Smirnov, A., O'Neill, N. T., Slutsker, I., and
768 Kinne, S.: Wavelength dependence of the optical depth of biomass burning, urban and
769 desert dust aerosols, J. Geophys. Res., 104, 31333–31349, doi:10.1029/1999JD90093,
770 1999.

771 Haywood, J.M.,Osborne, S.R., and Abel, S.J.: The effect of overlying absorbing aerosol layers
772 on remote sensing retrievals of cloud effective radius and cloud optical depth, *Q.J.R.*
773 Meterolog. Soc., 130, 779-800. Doi:10.1256/qj.03.100,2004.
774 Holben, B. N., Eck, T. F., Slutsker, I., Tanre, D., Buis, J. P., Setzer, A., Vermote, E., Reagan, J.
775 A.,Kaufman, Y. J., Nakajima, T., Lavenu, F., Jankowiak, I., and Smirnov, A.:
776 AERONET – a federated instrument network and data archive for aerosol
777 characterization, Remote Sens. Environ.,66, 1–16, 1998.
778 Holz, R. E., Ackerman, S. A., Nagle, F. W., Frey, R., Dutcher, S., Kuehn, R. E., Vaughan, M. A.,
779 and Baum, B.: Global Moderate Resolution Imaging and Spectroradiometer (MODIS)
780 cloud detection and height evaluation using CALIOP, J. Geophys. Res., 113,
781 D00A19,doi:10.1029/2008JD009837, 2008.
782 Hsu, N. C., Gautam, R., Sayer, A. M., Bettenhausen, C., Li, C., Jeong, M. J., Tsay, S.-C.,and
783 Holben, B. N.: Global and regional trends of aerosol optical depth over land and ocean
784 using SeaWiFS measurements from 1997 to 2010, Atmos. Chem. Phys., 12, 8037–8053,
785 15 doi:10.5194/acp-12-8037-2012, 2012.
786 Intergovernmental Panel on Climate Change (IPCC): The physical science basis, and
787 contribution of working group I to the fourth assessment report of the IPCC 916,
788 Cambridge Univ. Press.,2007
789 Kacenelebogen, M., Redemann, J., Vaughan, M. A., Omar, A. H., Russell, P. B., Burton, S.,
790 Rogers, R. R., Ferrare, R. A., and Hostetler, C. A.: An evaluation of
791 CALIOP/CALIPSO's aerosol-above-cloud detection and retrieval capability over North
792 America, J. Geophys. Res. Atmos., 119, 230–244, doi:10.1002/2013JD020178, 2014.

793 Kahn, R. A., Garay, M. J., Nelson, D. L., Levy, R. C., Bull, M. A., Diner, D. J., Martonchik, J.
794 V., Hansen, E. G., Remer, L. A., and Tanre, D.: Response to "Toward unified satellite
795 climatology and aerosol properties. 3. MODIS versus MISR AERONET", J. Quant.
796 Spectrosc. Ra., 112, 901–909, doi:10.1016/j.jqsrt.2010.11.001, 2011.
797 Kaufman, Y. J., Remer, L. A., Tanre, D., Li, R. R., Kleidman, R., Mattoo, S., Levy, R., Eck, T.,
798 Holben, B. N., Ichoku, C., Martins, J., and Koren, I.: A critical examination of the
799 residual cloud contamination and diurnal sampling effects on MODIS estimates of the
800 aerosol over ocean, IEEE T. Geosci. Remote, 43, 2886–2897, 2005a.
801 Kaufman, Y. J., Koren I., Remer, L.A., Tanre, D., Ginoux, P., and Fan, S.: Dust transport and
802 deposition observed from the Terra-Moderate Resolution Imaging Spectroradiometer
803 (MODIS) spacecraft over the Atlantic Ocean. J.Geophys.Res., 110, D10S12,
804 doi:10.1029/2003JD004436., 2005.
805 King, M. D., Tsay, S. C., Platnick, S. E., Menghua,W., and Liou, K. N.: Cloud retrievals
806 algorithm for MODIS: optical thickness, effective particle radius and thermodynamic
807 phase, Algorithm Theor. Basis Doc. ATBD-MOD-05, NASA Goddard Space Flight
808 Cent., Greenbelt, MD, 1997.
809 Leahy, L. V., Wood, R., Charlson, R. J., Hostetler, C. A., Rogers, R. R., Vaughan, M. A., and
810 Winker, D. M.: On the nature and extent of optically thin marine low clouds, J. Geophys.
811 Res., 117, D22201, doi:10.1029/2012JD017929, 2012.
812 Levy, R. C., Mattoo, S., Munchak, L. A., Remer, L. A., Sayer, A. M., Patadia, F., and Hsu, N.
813 C.: The Collection 6 MODIS aerosol products over land and ocean, Atmos. Meas. Tech.,
814 6, 2989–3034, doi:10.5194/amt-6-2989-2013, 2013.

Li, Z., Zhao, F., Liu, J., Jiang, M., Zhao, C., and Cribb, M.: Opposite effects of absorbing aerosols on the retrievals of cloud optical depth from spaceborne and ground-based measurements, J. Geophys. Res.-Atmos., 119, 5104–5114, doi:10.1002/2013JD021053, 2014.

Liu, Z., Vaughan, M.A., Winker, D.M., Kittaka, C., Getzewich, B., Kuehn, R., Omar, A., Powell, K., Treptie, C. and Hostetlet, C.: The CALIPSO Lidar Cloud and Aerosol Discrimination: Version 2 Algorithm and Initial Assessment of Performance, J. Atmos. Oceanic Technol., 26, 1198-1213, 2009.

Liu, Z., Winker, D. M., Omar, A. H., Vaughan, M. A., Kar, J., Trepte, C. R., and Hu, Y.: Evaluation of CALIOP 532-nm AOD over clouds, AGU Fall Meeting 2013, 2013.

Meyer, K., Platnick, S., Oreopoulos, L., and Lee, D.: Estimating the direct radiative effect of absorbing aerosols overlying marine boundary layer clouds in the southeast Atlantic using MODIS and CALIOP, J. Geophys. Res. Atmos., 118, 4801–4815, doi:10.1002/jgrd.50449, 2013.

Peters, K., Quaas, J., and Bellouin, N.: Effects of absorbing aerosols in cloudy skies: a satellite study over the Atlantic Ocean, Atmos. Chem. Phys., 11, 1393–1404, doi:10.5194/acp-11-1393-2011, 2011.

Platnick, S., Pincus, R., Wind, B., King, M. D., Gray, M. A., and Hubanks, P.: An initial analysis of the pixel-level uncertainties in the global MODIS cloud optical thickness and effective particle radius size retrievals, Proc. SPIE 5652, Passive Optical Remote Sensing of the Atmosphere and Cloud IV, 30, doi:10.1117/12.578353, 2004.

Powell., K. A., Hostetler, C. A., Liu, Z., Vaughan, M. A., Kuehn, R. E., Hunt, W. H., Lee, K. M., Trepte, C. R., Rogers, R. R., Young, S. A., and Winker, D. M.: CALIPSO lidar

calibration algorithms, part I: Nighttime 532,nm-parallel channel 532-nm perpendicular channel, J. Atmos.Ocean. Tech., 26, 2015–2033, 2009.

Remer, L. A., Kaufman, Y. J., Tanre, D., Mattoo, S., Chu, D. A., Martins, J. V., Li, R. R., Ichoku, C., Levy, R. C., Kleidman, R. G., Eck, T. F., Vermote, E., and Holben, B. N.: The MODIS aerosol algorithm, products and validation. J. Atmos. Sci., 62, 947–973, 2005.

Remer, L. A., Kleidman, R. G., Levy, R. C., Kaufman, Y. J., Tanre, D., Mattoo, S., Martins, J. V., Ichoku, C., Koren, I., Yu, H., and Holben, B. N.: Global aerosol climatology from MODIS satellite sensors, J. Geophys. Res., 113, D14S07, doi:10.1029/2007JD009661, 2008.

Roberts, G., Wooster, M. J., and Lagoudakis, E.: Annual and diurnal african biomass burning temporal dynamics, Biogeosciences, 6, 849–866, doi:10.5194/bg-6-849-2009, 2009.

Rossow, W. B. and Schiffer, R. A.: Advances in understanding clouds from ISCCP, B. Am. Meteorol. Soc., 80, 2261–2287, doi:10.1175/1520-04771999:080<2261:AIUCFI>2.0.CO;2, 1999.

Royal Netherlands Meteorological Society: Background information about Row Anomaly in OMI, available at: www.knmi.nl/omi/research/product/rowanomaly-background.php, accessed on December 22 2014

Sassen, K. and Cho, B. S.: Subvisual-thin cirrus lidar dataset for satellite verification and climatological research, J. Appl. Meteorol., 31, 1275–1285, 1992.

Satheesh, S. K., Morthy, K. K., Kaufman, Y. J., and Takemura, T.: Aerosol optical depth, physical properties and radiative forcing over the Arabian Sea, Meterol. Atmos. Phys., 91, 45–62, 2006.

861 Sayer, A. M., Hsu, N. C., Bettenhausen, C., Ahmad, Z., Holben, B. N., Smirnov, A., Thomas, G.
862 E., and Zhang, J.: SeaWiFS Ocean Aerosol Retrievals (SOAR): algorithm, validation,
863 and comparison with other datasets, J. Geophys. Res., 117, D03206,
864 doi:10.1029/2011JD016599, 2012.
865 Schrage, J. M. and Fink, A. H.: Nocturnal continental low-level stratus over Tropical West
866 Africa: observations and possible mechanisms controlling its onset, Mon. Weather Rev.,
867 140, 1794– 1809, doi:10.1175/MWR-D-11-00172.1, 2012.
868 Shi, Y., Zhang, J., Reid, J. S., Holben, B., Hyer, E. J., and Curtis, C.: An analysis of the
869 collection 5 MODIS over-ocean aerosol optical depth product for its implication in
870 aerosol assimilation, Atmos. Chem. Phys., 11, 557–565, doi:10.5194/acp-11-557-2011,
871 2011.
872 Smirnov, A., Holben, B. N., Giles, D. M., Slutsker, I., O'Neill, N. T., Eck, T. F., Macke, A.,
873 Croot, P., Courcoux, Y., Sakerin, S. M., Smyth, T. J., Zielinski, T., Zibordi, G., Goes, J.
874 I., Harvey, M. J., Quinn, P. K., Nelson, N. B., Radionov, V. F., Duarte, C. M., Losno, R.,
875 Sciare, J., Voss, K. J., Kinne, S., Nalli, N. R., Joseph, E., Krishna Moorthy, K., Covert,
876 D. S., Gulev, S. K., Milinevsky, G., Larouche, P., Belanger, S., Horne, E., Chin, M.,
877 Remer, L. A., Kahn, R. A., Reid, J. S., Schulz, M., Heald, C. L., Zhang, J., Lapina, K.,
878 Kleidman, R. G., Griesfeller, J., Gaitley, B. J., Tan, Q., and Diehl, T. L.: Maritime
879 aerosol network as a component of AERONET – first results and comparison with global
880 aerosol models and satellite retrievals, Atmos. Meas. Tech., 4, 583–597,
881 doi:10.5194/amt-4-583-2011, 2011.
882 Stephens, G. L., Vane, D. G., Boain, R. J., Mace, G. G., Sassen, K.,Wang, Z., Illingsworth, A. J.,
883 O'Connor, E. J., Rossow, W. B., Durden, S. L., Miller, S. D., Austin, R. T., Benedetti,

884 A., and Mitrescu, C.: The Cloudsat mission and the A-Train, B. Am. Meteorol. Soc., 83,
885 1771–1790, doi:10.1175/BAMS-83-12-1771, 2002.
886 Stevens, B. and Fetingold, G.: Untangling aerosol effects on clouds and precipitation in a
887 buffered system, Nature, 461, 607–613, 2009.
888 Thomason, L. W., Pitts, M. C., and Winker, D. M.: CALIPSO observations of stratospheric
889 aerosols: a preliminary assessment, Atmos. Chem. Phys., 7, 5283–5290, doi:10.5194/acp-
890 7-5283-2007, 2007.
891 Torres, O., Bhartia, P. K., Herman, J. R., and Ahmad, Z.: Derivation of aerosol properties from
892 satellite measurements of backscattered ultraviolet radiation: theoretical basis, J.
893 Geophys. Res., 103, 17110, doi:10.1029/98JD00900, 1998.
894 Torres, O., Tanskanen, A., Viehelmann, B., Ahn, C., Braak, R., Bhartia, P. K., Veefkind, P., and
895 Levelt, P.: Aerosols and surface UV products from Ozone Monitoring observations: an
896 overview, J. Geophys. Res., 112, D24S47, doi:10.1029/2007JD008809, 2007.
897 Torres, O., Jethva, H., and Bhartia, P. K.: Retrieval of aerosol optical depth above clouds from
898 OMI observations: sensitivity analysis and case studies. J. Atmos. Sci., 69, 1037–1053,
899 2012.
900 Toth, T. D.,Zhang, J.,Campbell, J.R., Reid J.S., Shi, Y.,Johnson, R.S.,Smirnov, A.,Vaughan,
901 M.A., and Winker, D.M.: Investigating enhanced Aqua MODIS aerosol optical depth
902 retrievals over the mid-to-high latitude Southern Oceans through intercomparison with
903 co-located CALIOP, MAN, and AERONET data sets, J. Geophys. Res. Atmos., 118,
904 4700–4714, doi:10.1002/jgrd.50311.,2013.

905 Waquet, F., Reidi, J., Labonnote, L. C., Goloub, P., Cairns, B., Deuze, J. L., and Tanre, D.:
906 Aerosol remote sensing over clouds using A-train observations, J. Atmos. Sci., 66, 2468–
907 2480, 2009.
908 Weatherhead, E. C., Reinsel, G. C., Tiao, G. C., Meng, X. L., Choi, D., Cheang, W. K., Keller,
909 T., DeLuisi, J., Wuebbles, D. J., Kerr, J. B., Miller, A. J., Oltmans, S. J., and Frederick, J.
910 E.: Factors affecting the detection of trends: statistical considerations and applications to
911 environmental data, J. Geophys. Res., 103, 17149–17161, 1998.
912 Wetherald, R. T. and Manabe, S.: Cloud feedback processes in a general circulation model J.
913 Atmos. Sci., 45, 1397–1415, 1988.
914 Wilcox, E. M.: Direct and semi-direct radiative forcing of smoke aerosols over clouds, Atmos.
915 Chem. Phys., 12, 139–149, doi:10.5194/acp-12-139-2012, 2012.
916 Wilcox, E. M., Harshvardian and Platnick, S.: Estimate of the impact of absorbing aerosol over
917 cloud on the MODIS retrievals of cloud optical thickness and effective radius using two
918 independent retrievals of liquid water path, J. Geophys. Res., 114, D05210,
919 doi:10.1029/2008JD010589, 2009.
920 Winker, D. M., Vaughan, M. A., Omar, A. H., Hu, Y., Powell, K. A., Liu, Z., Hunt, W. H., and
921 Young, S. A.: Overview of the CALIPSO mission and CALIOP data processing
922 Algorithm. J. Atmos. Ocean. Tech., 26, 2310–2323, doi:10.1175/2009TECHA.1281.1,
923 2009.
924 Winker, D. M. and coauthors.: The CALIPSO mission: a global 3D view of aerosols and clouds,
925 B. Am. Meteorol. Soc., 91, 1211–1229, 2010.
926 Wood, R.: Stratocumulus clouds, Mon. Weather Rev., 140, 2373–2423, 2012.

927 Yu, H., Dickinson, R., Chin, M., Kaufman, Y., Holben, B., Geogdzhayev, I., and Mischenko, M.:
928 Annual cycle of global distributions of aerosol optical depth from integration of MODIS
929 retrievals and GOCART model simulations, J. Geophys. Res., 108, 4128,
930 doi:10.1029/2002JD002717, 2003.
931 Yu, H., Zhang, Y., Chin, H., Liu, Z., Omar, A., Remer, L. A., Yang, Y., Yuan, T., and Zhang, J.:
932 An integrated analysis of aerosols above-clouds from A-train multi sensor measurements,
933 Remote Sens. Environ., 121, 125–131, 2012.
934 Zhang, J., Christopher, S. A., and Holben, B. N.: Intercomparison of smoke aerosol optical
935 thickness derived from GOES 8 imager and ground-based Sun photometers, J. Geophys.
936 Res., 106, 7387–7397, doi:10.1029/2000JD900540, 2001.
937 Zhang, J. and Reid, J. S.: MODIS aerosol product analysis for data assimilation: assessment of
938 level 2 aerosol optical thickness retrievals, J. Geophys. Res., 111, D222077,
939 doi:10.1029/2005JD006898, 2006.
940 Zhang, J. and Reid, J. S.: A decadal regional and global trend analysis of the aerosol optical
941 depth using a data-assimilation grade over-water MODIS and Level 2 MISR aerosol
942 products, Atmos. Chem. Phys., 10, 10949–10963, doi:10.5194/acp-10-10949-2010, 2010.
943 Zhang, J., Campbell, J. R., Reid, J. S., Westphal, D. L., Baker, N. L., Campbell, W. F., and Hyer,
944 E. J.: Evaluating the impact of assimilating CALIOP-derived aerosol extinction profiles
945 on a global mass transport model, Geophys. Res. Lett., 38, L14801,
946 doi:10.1029/2011GL047737, 2011.
947 Zhang, J., Reid, J. S., Campbell, J. R., Hyer, E. J., and Westphal, D. L.: Evaluating the impact of
948 multi-sensor data assimilation on a global aerosol particle transport model, J. Geophys.
949 Res. Atmos., 119, 4674–4689, doi:10.1002/2013JD020975, 2014.

950 Zhang, Z., Meyer, K., Platnick, S., Oreopoulos, L., Lee, D., and Yu, H.: A novel method for
951 estimating shortwave direct radiative effect of above-cloud aerosols using CALIOP and
952 MODIS data, Atmos. Meas. Tech., 7, 1777–1789, doi:10.5194/amt-7-1777-2014, 2014.
953

Figure Captions

Figure 1. (A-H) Multi-year (2006-2013) CALIOP-derived daytime global cloudy-sky ACA frequency applying different CALIOP AODs as the threshold between background and significant aerosol loading. The CALIOP AOD are binned into 2.5° x 2.5° bins derived using the CALIOP cloud and layer data sets. CALIOP AOD baseline thresholds of 0, 0.010, 0.015 and 0.020 are applied to Figs. 1A, 1B, 1C and 1D respectively for the Dec.-May period. Figures 1E-1H show the similar results as Fig. 1A-1D but for the June-Nov. period.

Figure 2. (A) Pairwise comparison between collocated OMI and CALIOP observations of above-cloud AI and AOD, respectively, as a function of the underlying MODIS cloud optical depth (COD). CALIOP AOD are averaged into OMI AI bins of 0.1. (B-I) Multi-year (2006-2013) daytime global cloudy-sky ACA frequency applying several different OMI AIs as the threshold between background and significant aerosol loading. The OMI AIs are binned into 1°x1° bins derived from the MODIS-OMI collocated data set. OMI AI baseline thresholds of 0.7, 0.8, 0.9 and 1.0 are applied to Figs. 2B, 2C, 2D and 2E respectively for the Dec.-May period. Figures 2F-2I depict the same information as Figs. 2B-2E for the June-Nov. period. ACA frequencies less than 5 % are shown in white.

Figure 3. (A) Seven year (December 2006- May 2013) daytime cloudy-sky frequency of occurrence of aerosol above-cloud events during December through May defined from OMI (ratio of totally cloudy MODIS pixels with AI greater than 1.0 to the number of totally cloudy MODIS pixels). (B) Day-time cloudy-sky frequency of occurrence of ACA events over cloudy skies from CALIOP (ratio of CALIOP pixels with CALIOP $AOD_{above\ cloud} > 0.015$ to the number of CALIOP pixels with column integrated COD > 0) for the

same temporal domain as Fig. 3A. (C) Night-time cloudy-sky frequency of occurrence defined similar to the daytime frequency from Fig. 3B. (D-F) Shows the same information as Figs. 3A-3C during June 2006-November 2013. Figures 3G-3H depict the ACA frequency ratio defined as the OMI-MODIS daytime cloudy-sky frequency divided by the CALIOP derived daytime cloudy-sky frequency for the December to May and June to November period, respectively. Figures 3I-3J depict the difference in cloudy-sky frequency used to construct the frequency ratio plots (3G and 3H) for the same temporal ranges. The red boxes show the areas selected for regional studies. Only OMI and CALIOP bins with frequency of 5% or higher are shown in this analysis.

Figure 4. (a) Aqua MODIS true color image on July 8, 2007 over the Saharan Desert in Northern Africa (b) The same domain as Figure 4a but for Cloud Fraction from the MODIS MYD06 data. (c) Similar to Figure 3a but for OMI Aerosol Index (AI). Fig. 4c is created by averaging all OMI observations into 0.25° x 0.25° grids over the region shown. (d) The vertical profile for CALIOP backscatter, where the instrument overpass is superimposed on Figure 4a. Also, the CALIOP track shown in Fig. 4a is constructed by highlighting those MODIS observations that are collocated with CALIOP observations.

Figure 5. (A) Multi-year (2006-2013) daytime AI averaged into 1.0° x1.0° bins constructed from collocated MODIS and OMI AI over strictly MODIS cloudy scenes during December through May. The averaged OMI AI is neglected below 1.0 in accordance with the AI ground floor determined in Fig. 2. (B) Multi-year (2006-2013) daytime ACAOD averaged into 2.5° x 2.5° bins derived from CALIOP cloud and aerosol layer products. Averaged CALIOP ACAOD below 0.015 are considered below the noise floor for the study and thus are not shown. (C) Shows the CALIOP ACAOD similar to Fig. 5B except

for night-time observations. (D-F) Shows the same information as Figs. 5A-5C during the summer and fall months (June-November).

Figure 6. Multi-year (June 2006 - November 2013) frequency of occurrence of low-level clouds defined by CALIOP as the ratio of pixels with COD greater than 0 with cloud-top height < 3km to the total number of CALIOP scenes within the current 2.5° x 2.5° bin for (A) December to May during daytime observations, (B) December to May of night-time observations, (C) Daytime frequency of occurrence of low-level cloud decks defined similar to Fig 6A. during the June-November time frame and (D). Nighttime frequency of occurrence of low-level cloud decks for the same time frame as Fig. 6C. Figures 6E and 6F depict the night to daytime frequency ratio for the December to May and June to November periods, respectively.

Figure 7. Multi-year (2006-2013) 2.5° x 2.5° averaged CALIOP day-time AOD for (A) December through May over completely cloud free scenes derived from CALIOP cloud and aerosol layer daytime analysis, (B) Nighttime analysis during the December to May period, (C) Daytime analysis for the June to November period and (D) nighttime analysis for the June to November period. Only scenes which contained an averaged AOD > 0.2 with a column COD = 0 were used in the analysis.

Figure 8. (A) Two-and-a-half-year (June 2006 – November 2008) daytime CALIOP cloudy-sky ACA frequency during the December through May period, using the collocated OMI-MODIS-CALIOP dataset (defined in Table 1). (B) The same as Fig. 8A, however for the all-sky CALIOP ACA frequency. (C) CALIOP cloudy sky frequency, which is defined as the number of collocated CALIOP observations with COD > 0 over the total number of collocated CALIOP observations. (D-F) Similar to Figs. 8a-8c but using the OMI-

MODIS-based method (defined in Table 1). It should be noted that the cloudy sky frequency from the OMI-MODIS technique is defined as the number of observations with cloud fraction equals to one divided by the total number of observations (defined in Table 1). (G-J) Depict the same information as 8A-F except for the June – November (2006-2008) period.

Figure 9. (A) Two-and-a-half-year (June 2006 – November 2008) daytime CALIOP cloudy-sky frequency during the December through May period, using the collocated OMI-MODIS-CALIOP dataset with the application of the most lenient cloud QA. (B-C) Depict the same information as Fig. 9A, however now using intermediate and strict cloud QA settings, respectively. (D) Depicts the all-sky frequency using the same data set as Fig. 9A, now using lenient cloud and aerosol QAs. (E-F) Depict the same information as Fig. 9D varying the cloud QA to intermediate and strict. (G-I) Similar to Figs. D-F but holding the lenient cloud QA while varying the aerosol QA from lenient to intermediate and strict, respectively. (J-R) Depict the same information as Figs. 9A-I for the June to November period (2006 – 2008).

Figure 10. Monthly-averaged global ACA frequencies derived using the OMI-MODIS based method (green) as well as the CALIOP-based method as described in the text. The corresponding baseline thresholds are applied to both CALIOP and OMI data. Dashed lines represent monthly variations in ACA frequencies and the solid lines represent the yearly ACA frequency trends: OMI daytime cloudy-sky frequency is shown in green, CALIOP nighttime cloudy-sky frequency is orange, CALIOP nighttime all-sky frequency is purple, CALIOP daytime cloudy-sky frequency is red and CALIOP daytime all-sky frequency is blue.

Figure 11. (A) A single swath from the OMI instrument over northern Africa on August 1, 2007 before the significant data loss reported in all OMI aerosol products. (B) A single OMI AI swath over the same region as Fig. 11A on June 1, 2009 which is affected by the significant data loss.

Figure 12. The OMI AI as a function of the sensor's viewing zenith angle (VZA). All OMI AI data over the course of a year (2007) were binned into 1° VZA increments. The red vertical bars represent the 95% confidence interval for each 1° bin.

Figure 13. Monthly-averaged over ocean clear-sky AODs derived from collocated CALIOP and AERONET data. CALIOP retrievals within 0.3° latitude and longitude and ± 30 minutes of the corresponding AERONET station and observation are considered collocated. AERONET and CALIOP AODs above 0.2 and 0.6, respectively, are not included in order to avoid high aerosol loading cases and exclude noisy CALIOP data.

Figure 14. Monthly-averaged global CALIOP cloudy-sky frequencies after applying several different threshold techniques to both day and night time data. The solid lines show the daytime scenario for each respective case while the dotted lines show the nighttime observations for each case.

Figure 15. The de-seasonalized monthly- and regionally-averaged cloudy-sky frequency of ACA occurrences for the nine different regions outlined in Fig. 3 and explained in Table 3. The dashed lines show the monthly frequency over the regions and the solid lines show the trend lines computed for each region with the x-axis representing the year of the study. The CALIOP nighttime analysis is shown in aqua marine and the day-time analysis is shown in dark blue.

Table Captions

Table 1. Various definitions of frequency of above-cloud aerosols (ACA) used throughout the study.

Table 2. Global cloudy-sky relative frequency and data counts for the sensitivity test carried out in Sect. 5. Aerosol and cloud layers retrieved with 'intermediate' or 'strict' QA metrics are considered in this analysis. A total of five different threshold tests are applied to both day and nighttime CALIOP cloud and aerosol layer products.

Table 3 Seven and a half year above-cloud aerosol cloudy-sky frequency, ACAOD and clear-sky AOD inter-annual variability analysis for the selected target regions. Aerosol and cloud layers retrieved with 'intermediate' or 'strict' QA metrics are considered in this analysis. Yearly variation for the entire globe is also included. For each region, inter-annual variability (frequency change per year) for the three parameters, the ACA cloudy-sky frequency, ACAOD and clear-sky AOD values are reported. Note that the inter-annual variability for clear sky AODs is estimated using 100% cloud free data from the CALIOP cloud and aerosol layer products.

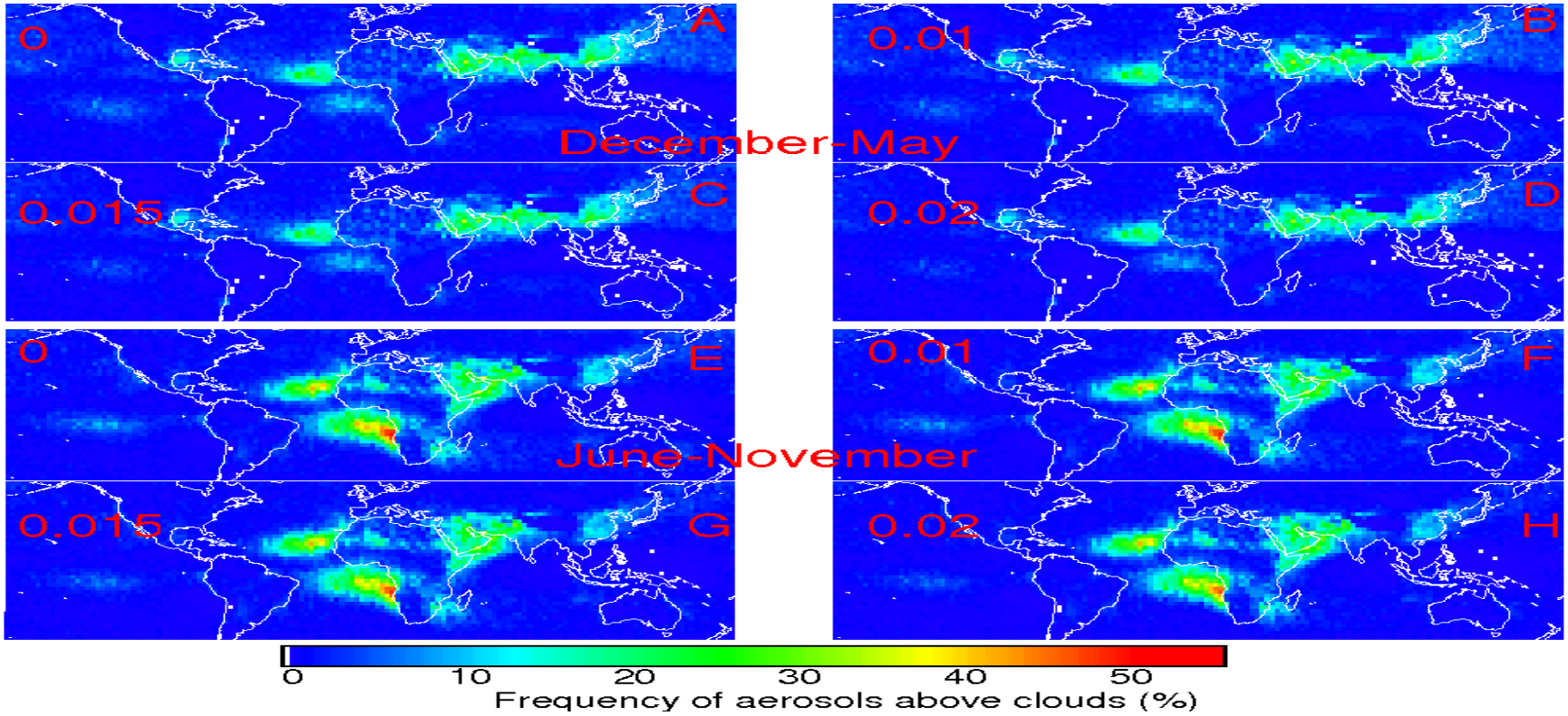

Figure 1. (A-H) Multi-year (2006-2013) CALIOP-derived daytime global cloudy-sky ACA frequency applying different CALIOP AODs as the threshold between background and significant aerosol loading. The CALIOP AOD are binned into 2.5° x 2.5° bins derived using the CALIOP cloud and layer data sets. CALIOP AOD baseline thresholds of 0, 0.010, 0.015 and 0.020 are applied to Figs. 1A, 1B, 1C and 1D respectively for the Dec.-May period. Figures 1E-1H show the similar results as Fig. 1A-1D but for the June-Nov. period.

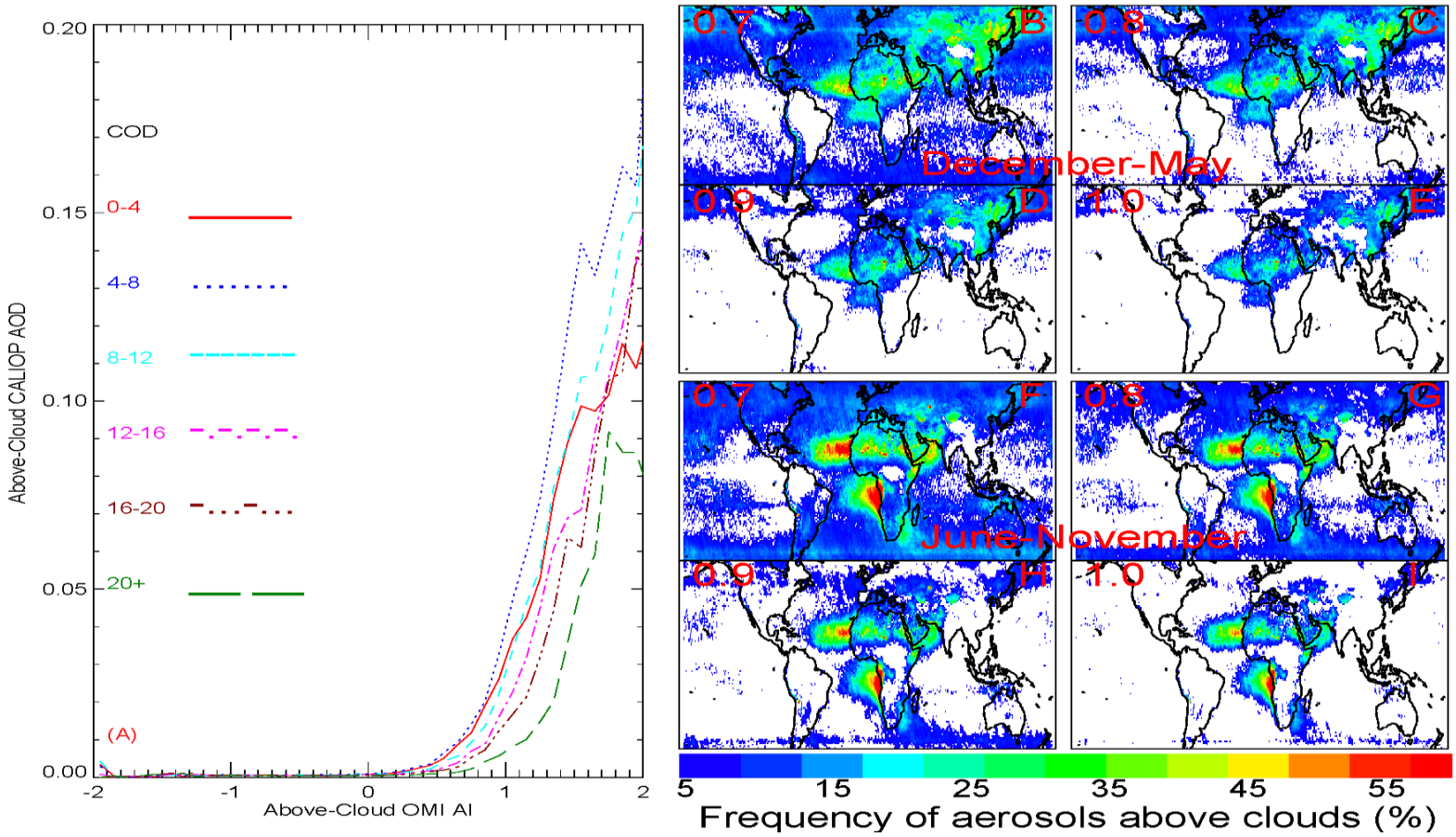

Figure 2. (A) Pairwise comparison between collocated OMI and CALIOP observations of above-cloud AI and AOD, respectively, as a function of the underlying MODIS cloud optical depth (COD). CALIOP AOD are averaged into OMI AI bins of 0.1. (B-I) Multi-year (2006-2013) daytime global cloudy-sky ACA frequency applying several different OMI AIs as the threshold between background and significant aerosol loading. The OMI AIs are binned into 1°x1° bins derived from the MODIS-OMI collocated data set. OMI AI baseline thresholds of 0.7, 0.8, 0.9 and 1.0 are applied to Figs. 2B, 2C, 2D and 2E respectively for the Dec.-May period. Figures 2F-2I depict the same information as Figs. 2B-2E for the June-Nov. period. ACA frequencies less than 5 % are shown in white.

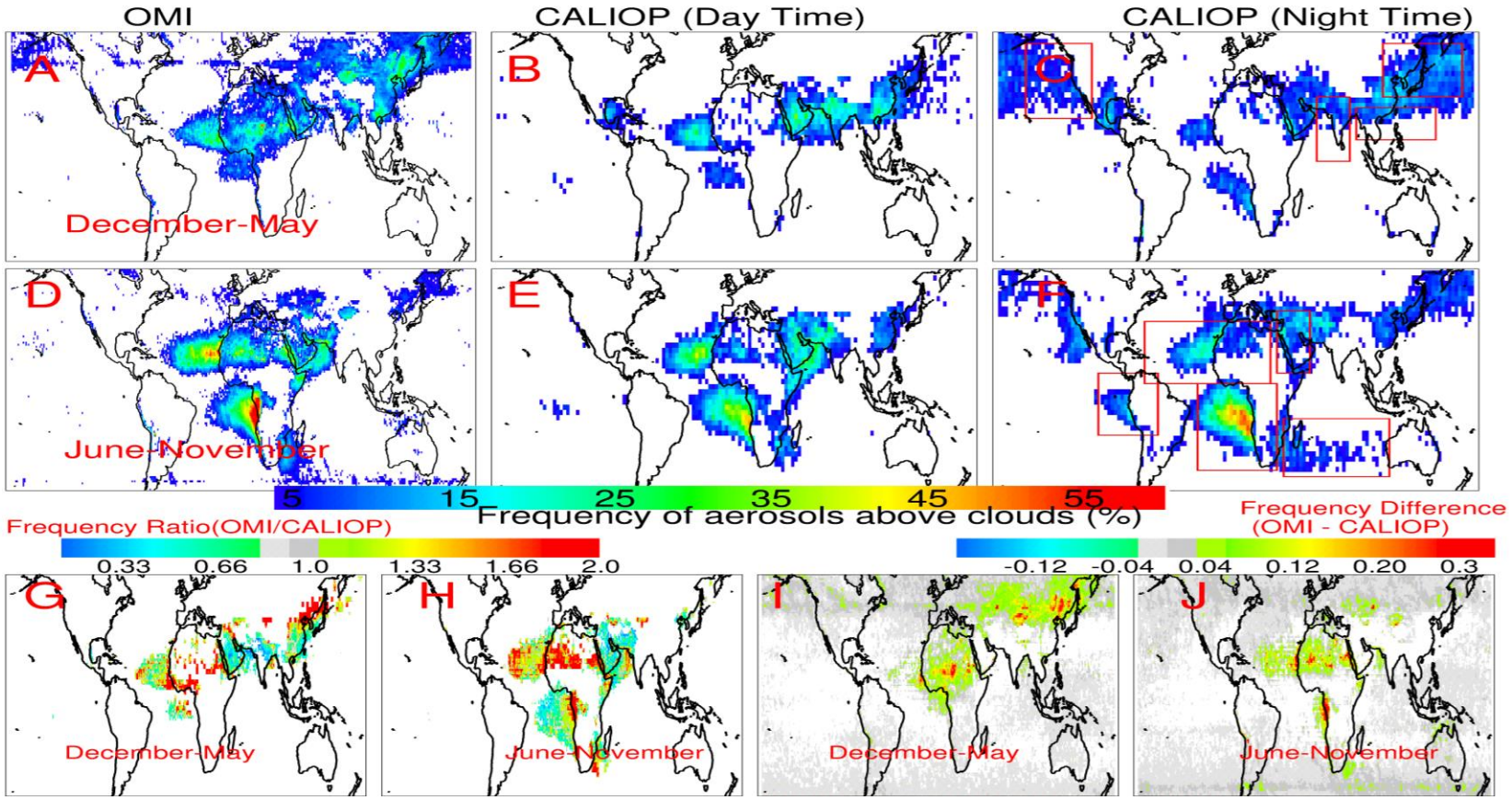

Figure 3. (A) Seven year (December 2006- May 2013) daytime cloudy-sky frequency of occurrence of aerosol above-cloud events during December through May defined from OMI (ratio of totally cloudy MODIS pixels with AI greater than 1.0 to the number of totally cloudy MODIS pixels). (B) Day-time cloudy-sky frequency of occurrence of ACA events over cloudy skies from CALIOP (ratio of CALIOP pixels with CALIOP $AOD_{above\ cloud} > 0.015$ to the number of CALIOP pixels with column integrated COD > 0) for the same temporal domain as Fig. 3A. (C) Night-time cloudy-sky frequency of occurrence defined similar to the daytime frequency from Fig. 3B. (D-F) Shows the same information as Figs. 3A-3C during June 2006-November 2013. Figures 3G-3H depict the ACA frequency ratio defined as the OMI-MODIS daytime cloudy-sky frequency divided by the CALIOP derived daytime cloudy-sky frequency for the December to May and June to November period, respectively. Figures 3I-3J depict the difference in cloudy-sky frequency used to construct the frequency ratio plots (3G and 3H) for the same temporal ranges. The red boxes show the areas selected for regional studies. Only OMI and CALIOP bins with frequency of 5% or higher are shown in this analysis.

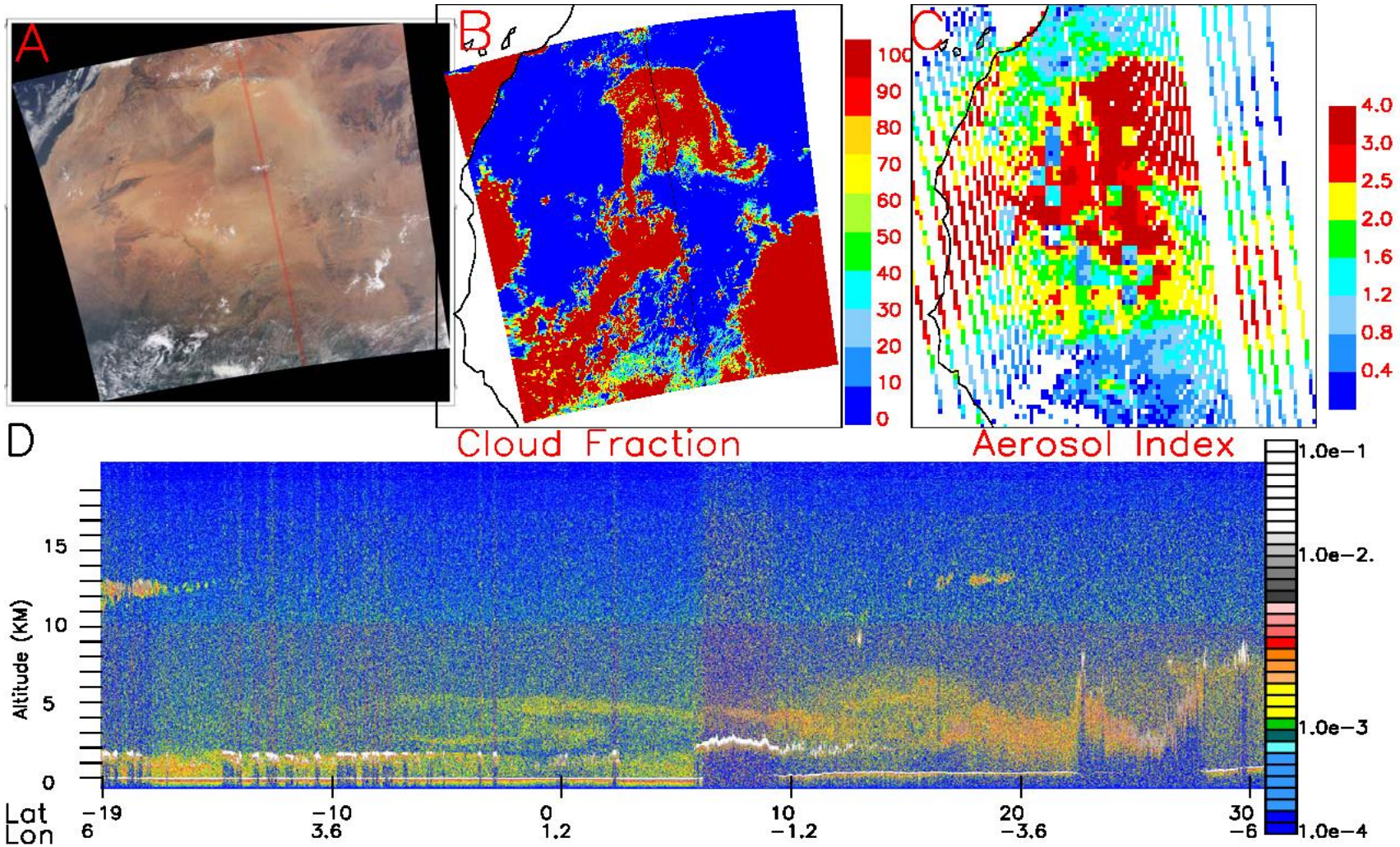

Figure 4. (a) Aqua MODIS true color image on 8 July 2007 over the Saharan Desert in Northern Africa (b) The same domain as Figure 4a but for Cloud Fraction from the MODIS MYD06 data. (c) Similar to Figure 3a but for OMI Aerosol Index (AI). Fig. 4c is created by averaging all OMI observations into 0.25° x 0.25° grids over the region shown. (d) The vertical profile for CALIOP backscatter, where the instrument overpass is superimposed on Figure 4a. Also, the CALIOP track shown in Fig. 4a is constructed by highlighting those MODIS observations that are collocated with CALIOP observations.

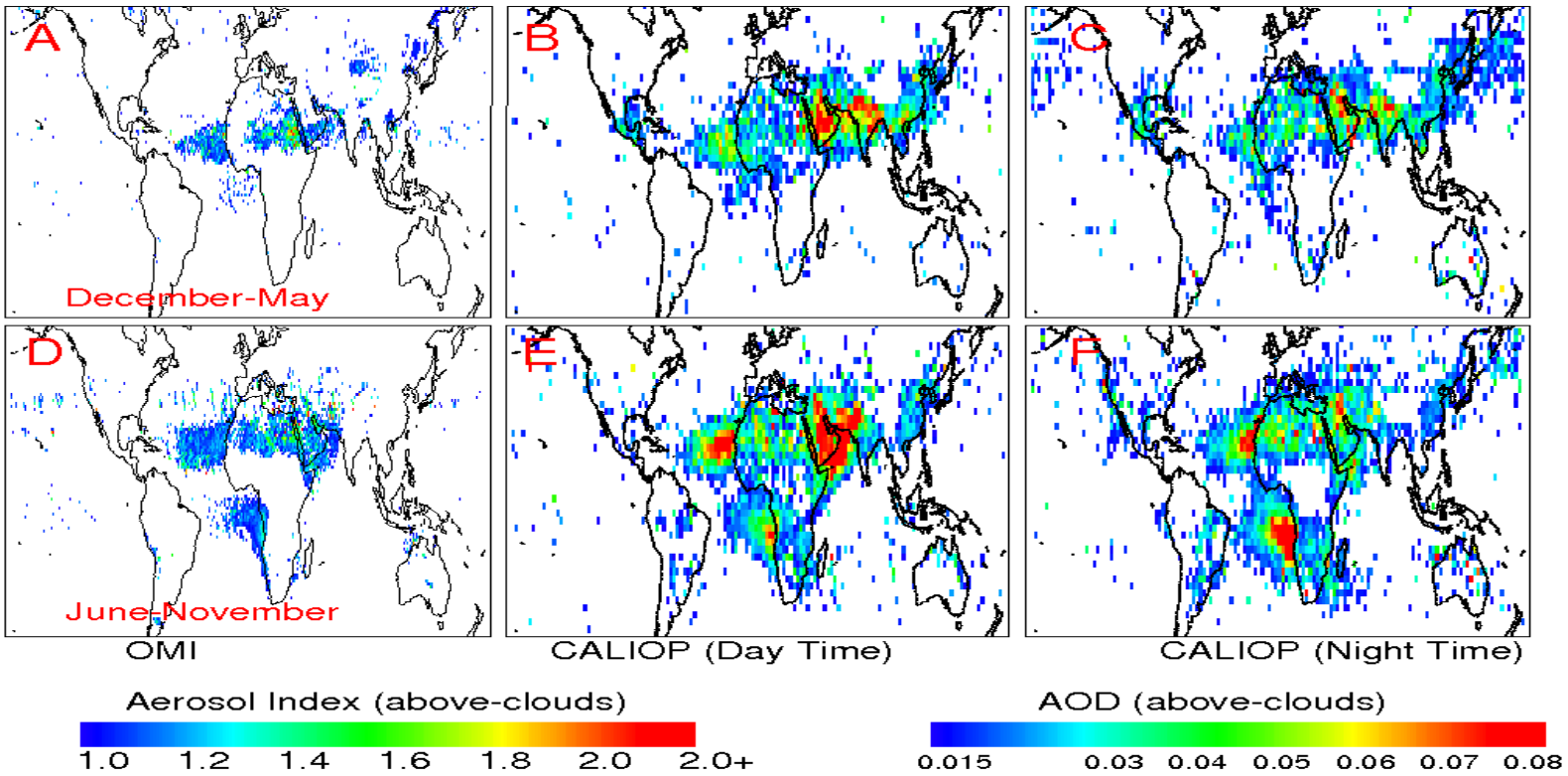

Figure 5. (A) Multi-year (2006-2013) daytime AI averaged into 1.0° x1.0° bins constructed from collocated MODIS and OMI AI over strictly MODIS cloudy scenes during December through May. The averaged OMI AI is neglected below 1.0 in accordance with the AI ground floor determined in Fig. 2. (B) Multi-year (2006-2013) daytime ACAOD averaged into 2.5° x 2.5° bins derived from CALIOP cloud and aerosol layer products. Averaged CALIOP ACAOD below 0.015 are considered below the noise floor for the study and thus are not shown. (C) Shows the CALIOP ACAOD similar to Fig. 5B except for night-time observations. (D-F) Shows the same information as Figs. 5A-5C during the summer and fall months (June-November).

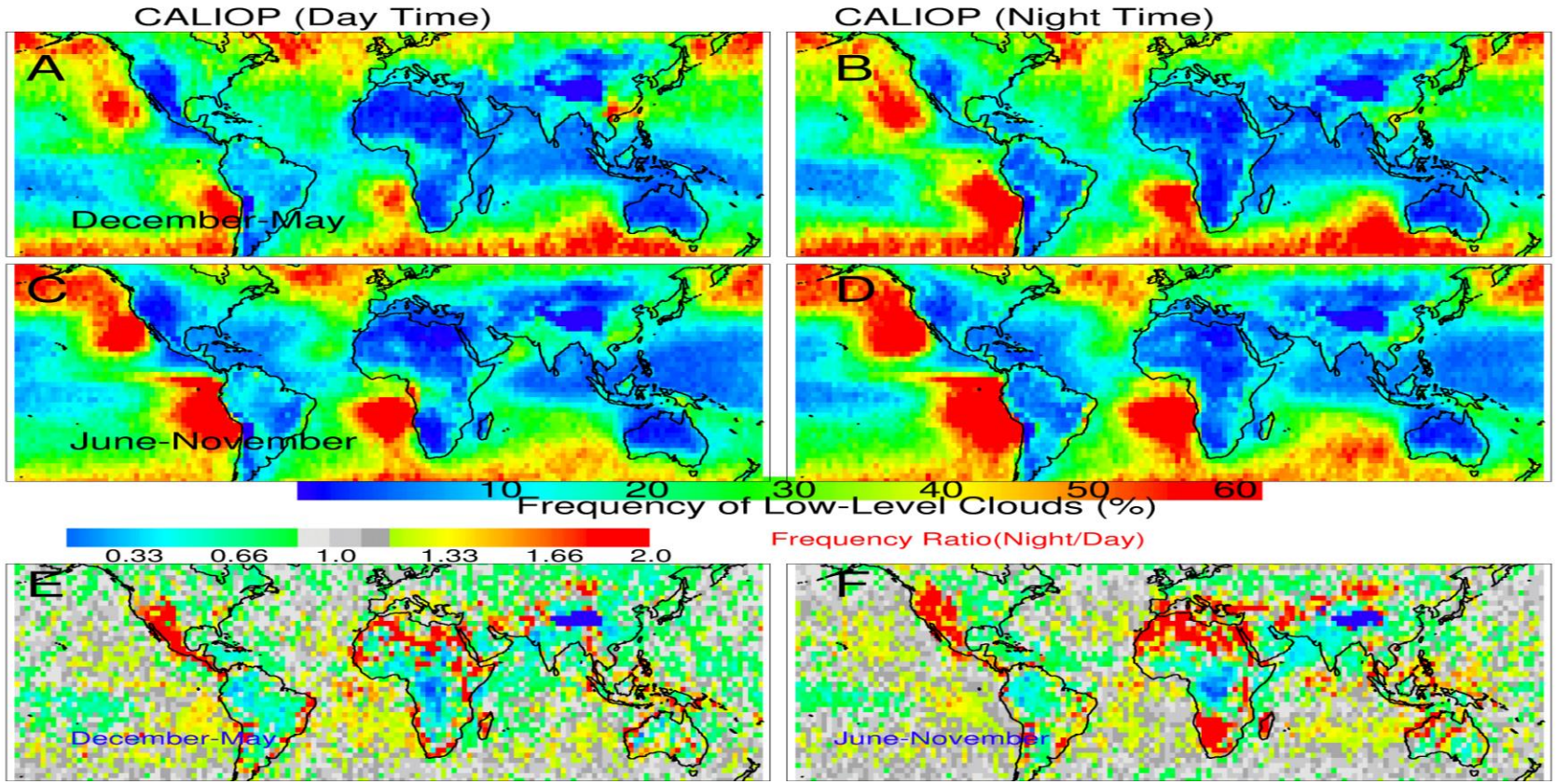

Figure 6. Multi-year (June 2006 - November 2013) frequency of occurrence of low-level clouds defined by CALIOP as the ratio of pixels with COD greater than 0 with cloud-top height < 3km to the total number of CALIOP scenes within the current 2.5° x 2.5° bin for (A) December to May during daytime observations, (B) December to May of night-time observations, (C) Daytime frequency of occurrence of low-level cloud decks defined similar to Fig 6A. during the June-November time frame and (D). Nighttime frequency of occurrence of low-level cloud decks for the same time frame as Fig. 6C. Figures 6E and 6F depict the night to daytime frequency ratio for the December to May and June to November periods, respectively.

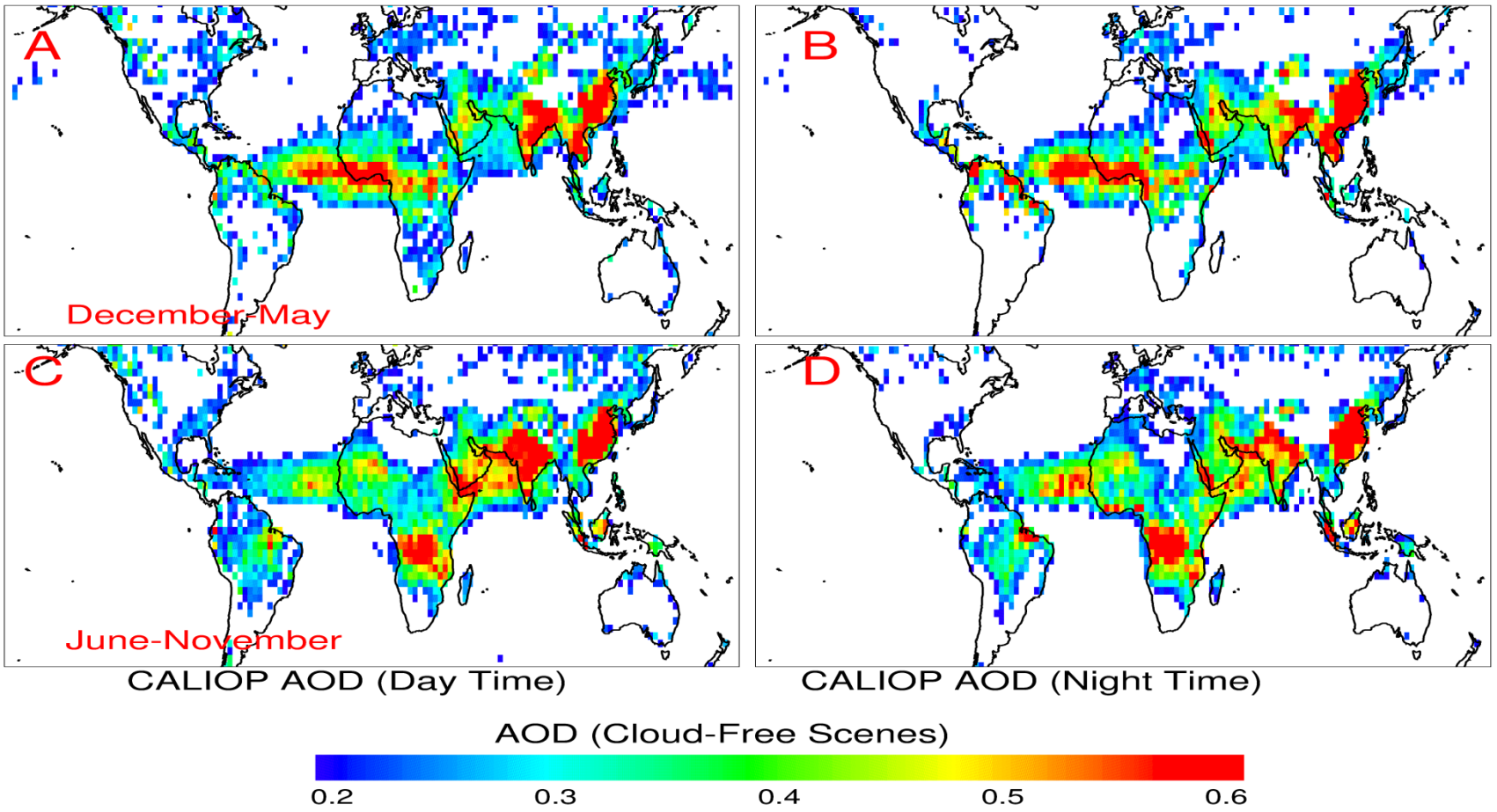

Figure 7. Multi-year (2006-2013) 2.5° x 2.5° averaged CALIOP day-time AOD for (A) December through May over completely cloud free scenes derived from CALIOP cloud and aerosol layer daytime analysis, (B) Nighttime analysis during the December to May period, (C) Daytime analysis for the June to November period and (D) nighttime analysis for the June to November period. Only scenes which contained an averaged AOD > 0.2 with a column COD = 0 were used in the analysis.

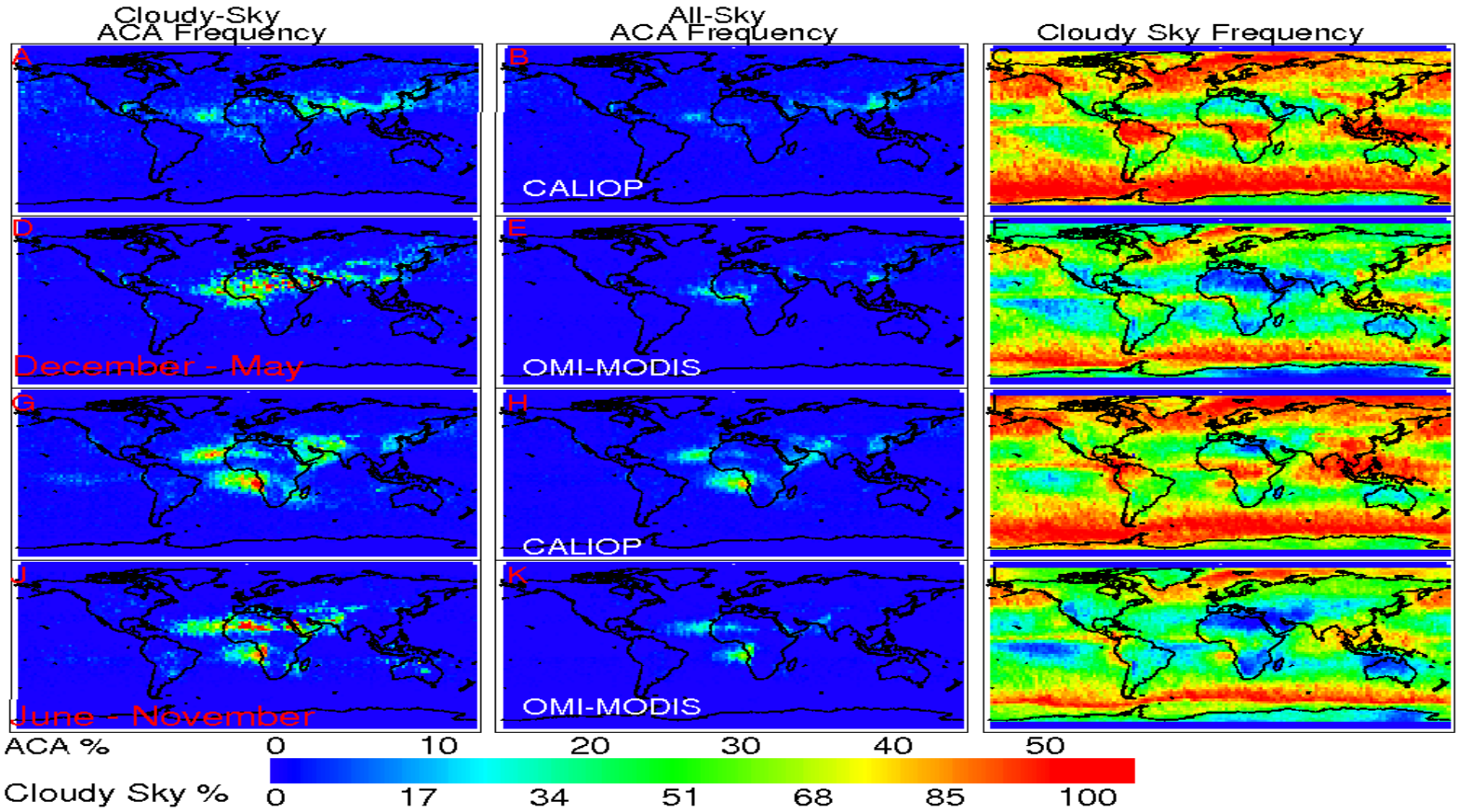

Figure 8. (A) Two-and-a-half-year (June 2006 – November 2008) daytime CALIOP cloudy-sky ACA frequency during the December through May period, using the collocated OMI-MODIS-CALIOP dataset (defined in Table 1). (B) The same as Fig. 8A, however for the all-sky CALIOP ACA frequency. (C) CALIOP cloudy sky frequency, which is defined as the number of collocated CALIOP observations with COD > 0 over the total number of collocated CALIOP observations. (D-F) Similar to Figs. 8a-8c but using the OMI-MODIS-based method (defined in Table 1). It should be noted that the cloudy sky frequency from the OMI-MODIS technique is defined as the number of observations with cloud fraction equals to one divided by the total number of observations (defined in Table 1.) (G-J) Depict the same information as 8A-F except for the June – November (2006-2008) period.

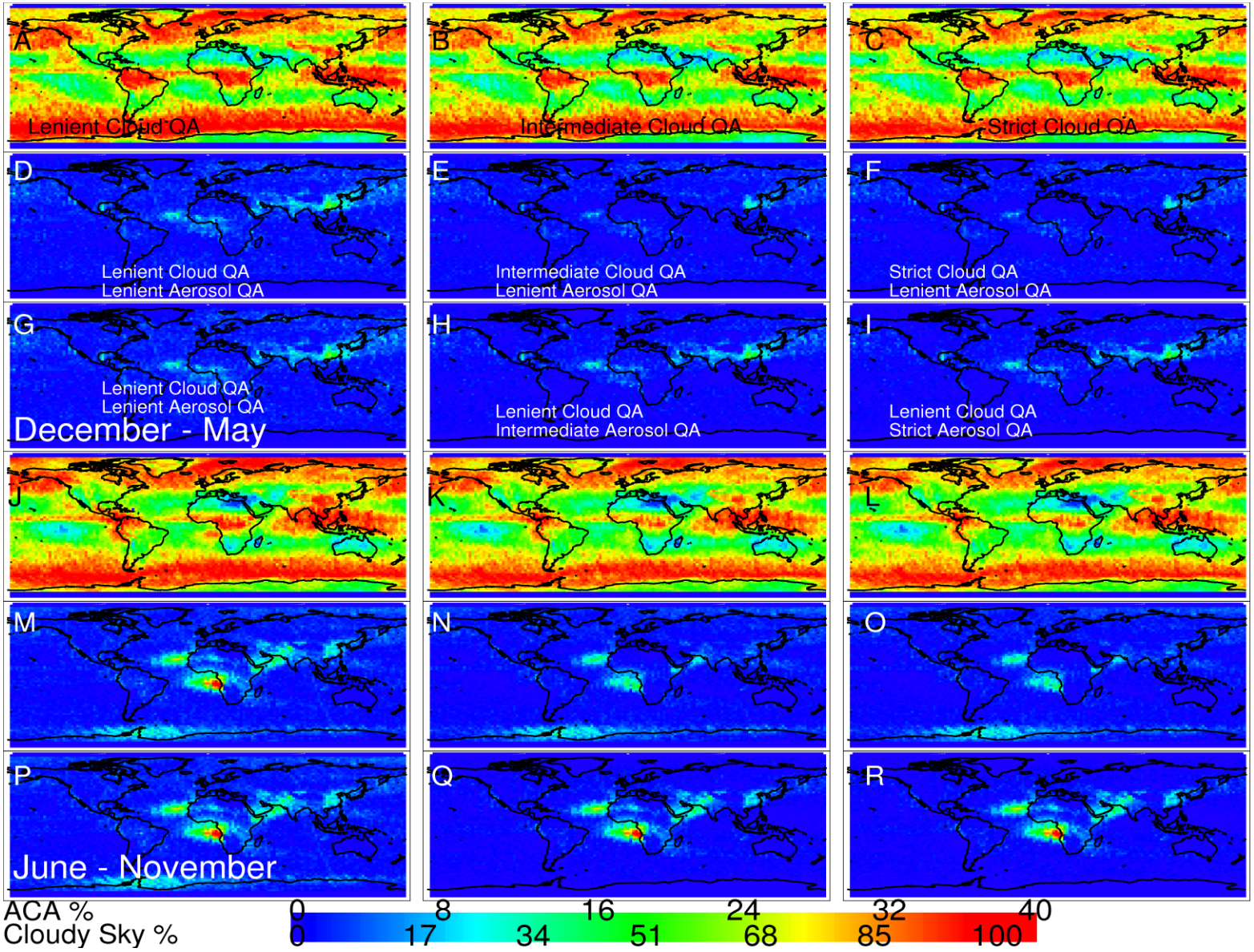
A
Lenient Cloud QA
B
Intermediate Cloud QA
C
Strict Cloud QA
D
Lenient Cloud QA
Lenient Aerosol QA
E
Intermediate Cloud QA
Lenient Aerosol QA
F
Strict Cloud QA
Lenient Aerosol QA
G
Lenient Cloud QA
Lenient Aerosol QA
December - May
H
Lenient Cloud QA
Intermediate Aerosol QA
I
Lenient Cloud QA
Strict Aerosol QA
J
K
L
M
N
O
P
June - November
Q
R
ACA %
0
8
16
24
32
40
Cloudy Sky %
0
17
34
51
68
85
100

Figure 9. (A) Two-and-a-half-year (June 2006 – November 2008) daytime CALIOP cloudy-sky frequency during the December through May period, using the collocated OMI-MODIS-CALIOP dataset with the application of the most lenient cloud QA. (B-C) Depict the same information as Fig. 9A, however now using intermediate and strict cloud QA settings, respectively. (D) Depicts the all-sky frequency using the same data set as Fig. 9A, now using lenient cloud and aerosol QAs. (E-F) Depict the same information as Fig. 9D varying the cloud QA to intermediate and strict. (G-I) Similar to Figs. D-F but holding the lenient cloud QA while varying the aerosol QA from lenient to intermediate and strict, respectively. (J-R) Depict the same information as Figs. 9A-I for the June to November period (2006 – 2008).

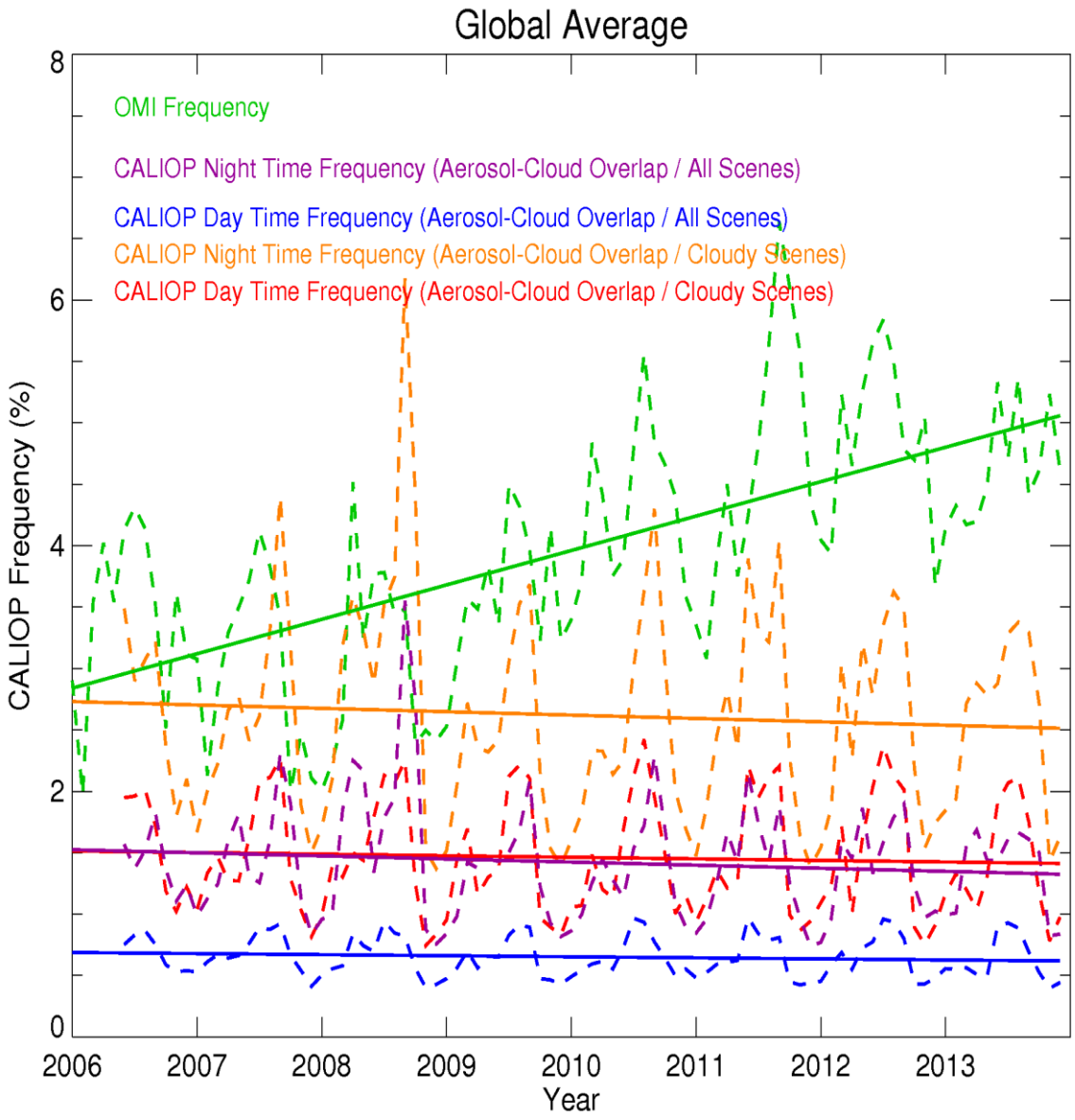

Figure 10. Monthly-averaged global ACA frequencies derived using the OMI-MODIS based method (green) as well as the CALIOP-based method as described in the text. The corresponding baseline thresholds are applied to both CALIOP and OMI data. Dashed lines represent monthly variations in ACA frequencies and the solid lines represent the yearly ACA frequency trends: OMI daytime cloudy-sky frequency is shown in green, CALIOP nighttime cloudy-sky frequency is orange, CALIOP nighttime all-sky frequency is purple, CALIOP daytime cloudy-sky frequency is red and CALIOP daytime all-sky frequency is blue.

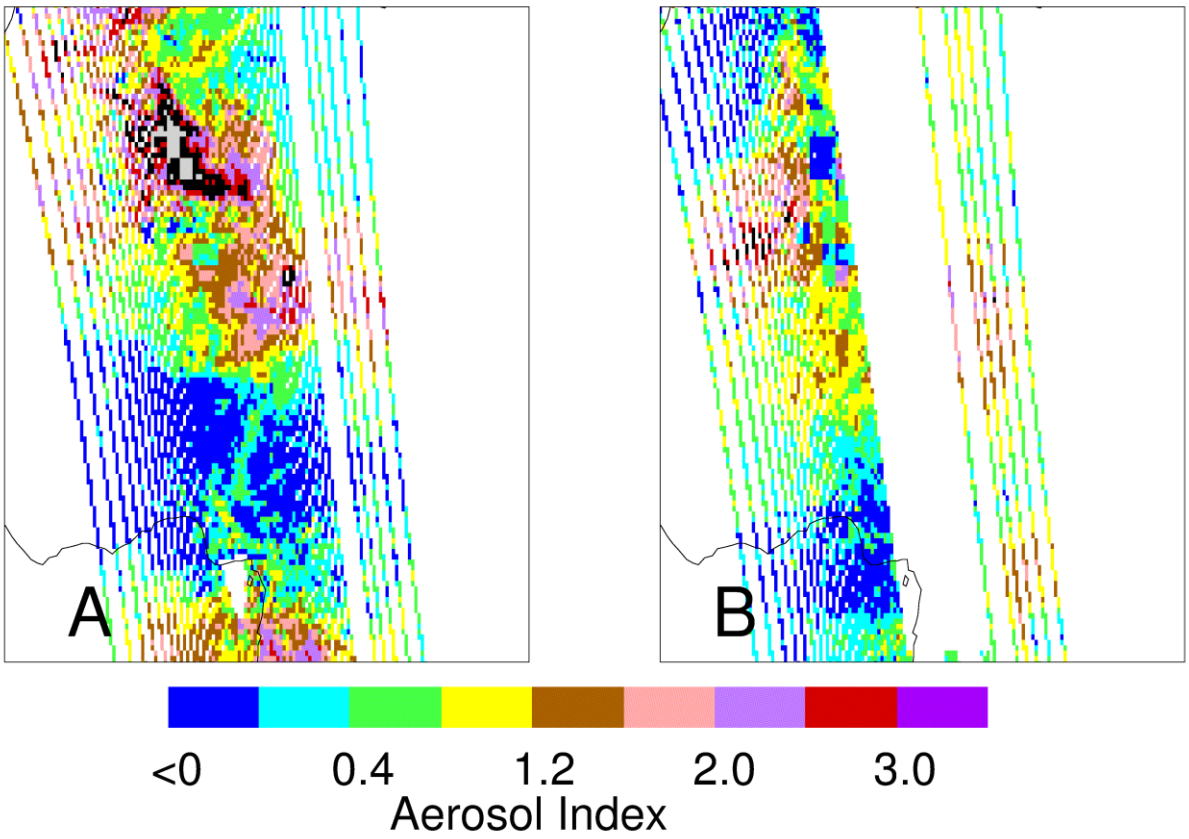

Figure 11. (A) A single swath from the OMI instrument over northern Africa on August 1, 2007 before the significant data loss reported in all OMI aerosol products. (B) A single OMI AI swath over the same region as Fig. 11A on June 1, 2009 which is affected by the significant data loss

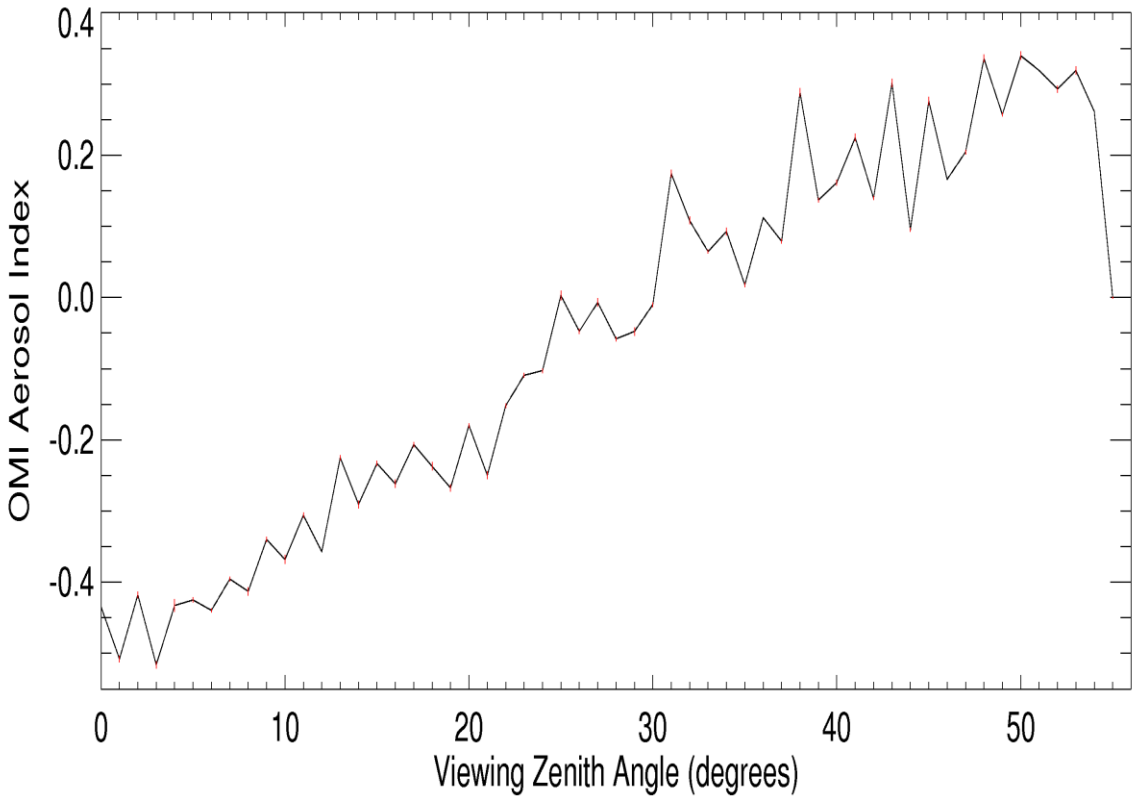

Figure 12. The OMI AI as a function of the sensor's viewing zenith angle (VZA). All OMI AI data over the course of a year (2007) were binned into 1° VZA increments. The red vertical bars represent the 95% confidence interval for each 1° bin.

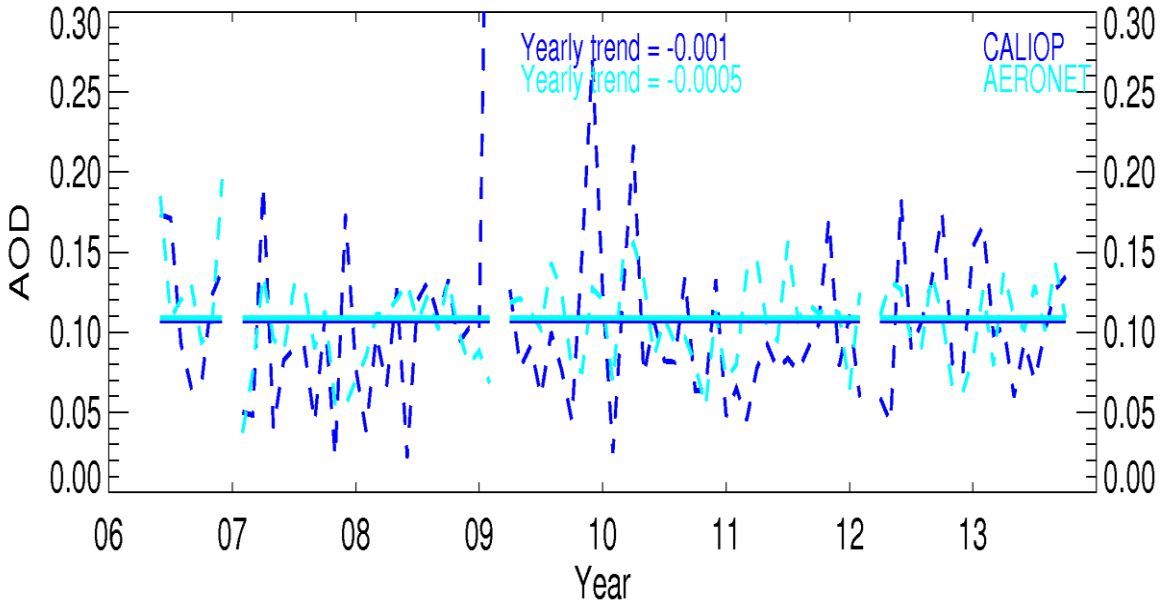

Figure 13. Monthly-averaged over ocean clear-sky AODs derived from collocated CALIOP and AERONET data. CALIOP retrievals within 0.3° latitude and longitude and ± 30 minutes of the corresponding AERONET station and observation are considered collocated. AERONET and CALIOP AODs above 0.2 and 0.6, respectively, are not included in order to avoid high aerosol loading cases and exclude noisy CALIOP data.

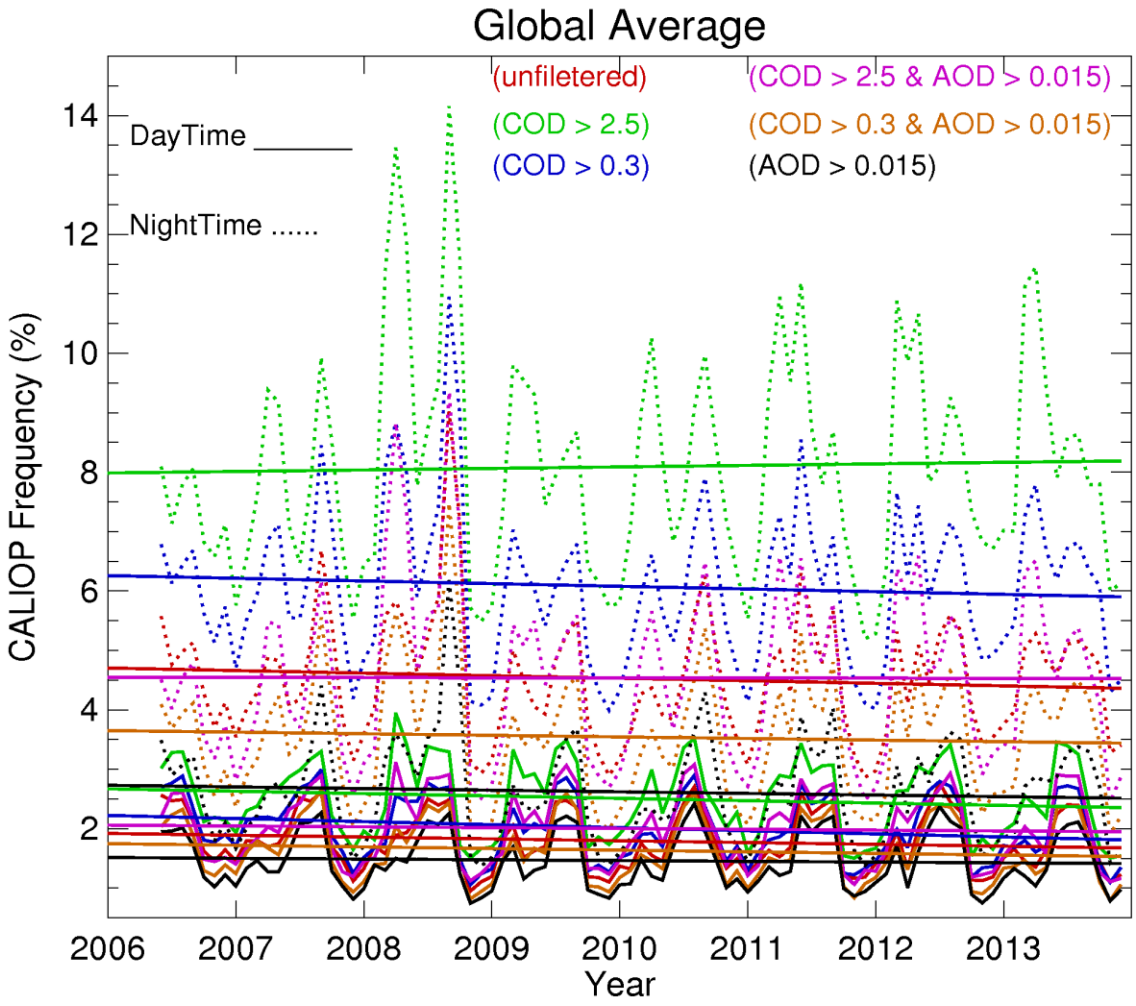

Figure 14. Monthly-averaged global CALIOP cloudy-sky frequencies after applying several different threshold techniques to both day and night time data. The solid lines show the daytime scenario for each respective case while the dotted lines show the nighttime observations for each case.

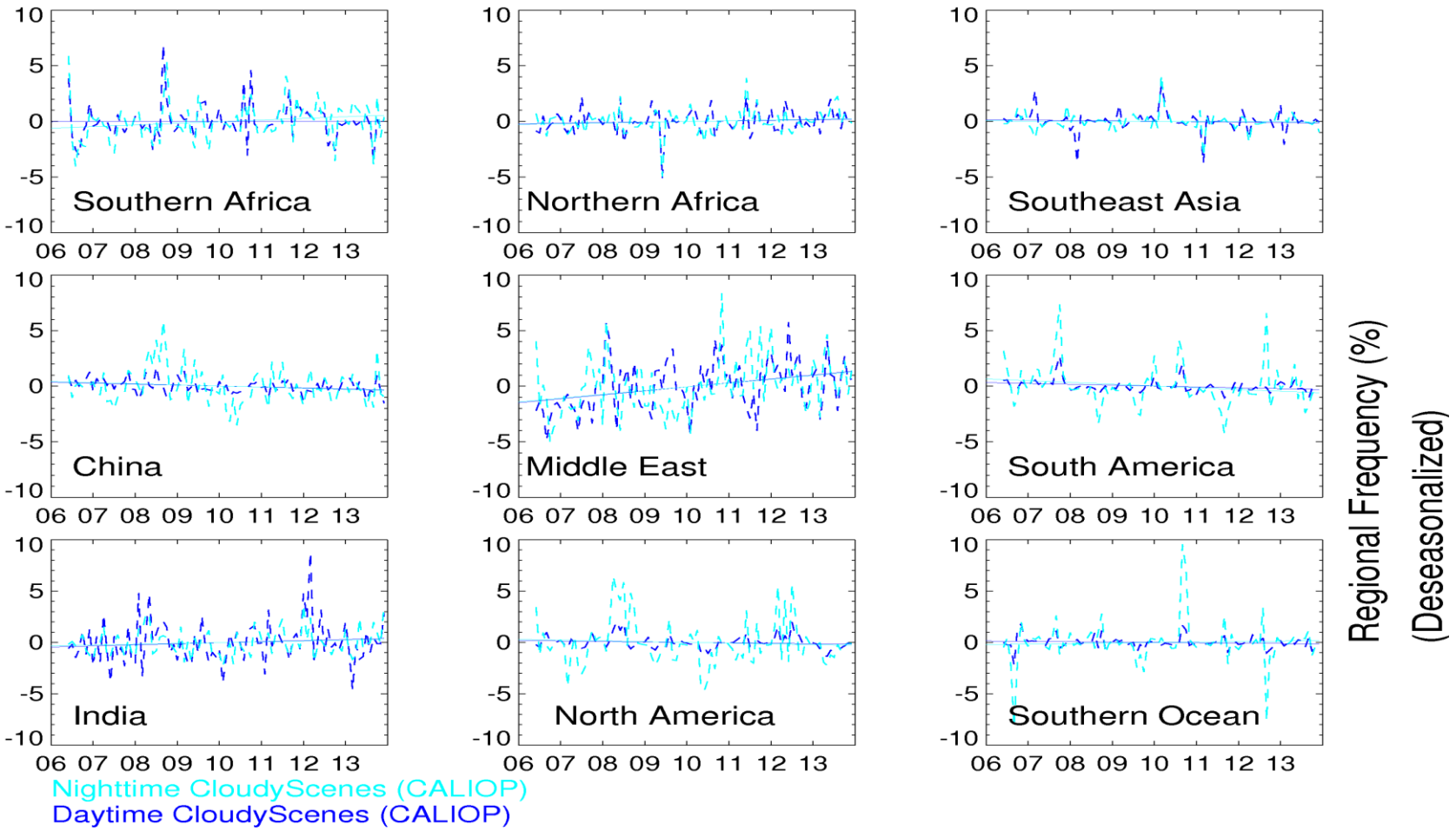

Figure 15. The de-seasonalized monthly- and regionally-averaged cloudy-sky frequency of ACA occurrences for the nine different regions outlined in Fig. 3 and explained in Table 3. The dashed lines show the monthly frequency over the regions and the solid lines show the trend lines computed for each region with the x-axis representing the year of the study. The CALIOP nighttime analysis is shown in aqua marine and the day-time analysis is shown in dark blue.

Table 1. Various definitions of frequency of above-cloud aerosols (ACA) used throughout the study.

Name	Data Set	Definition
Cloudy-Sky ACA Frequency (Passive)	OMI-MODIS	(# of MODIS observation with assigned AI > AI baseline and cloud fraction equal to one) / (# of MODIS observations with cloud fraction equal to one and valid AI retrieval) per latitude and longitude grid over given time period
All-Sky ACA Frequency (Passive)	OMI-MODIS	(# of MODIS observation with assigned AI > AI baseline and cloud fraction equal to one) / (# of MODIS observations with valid AI retrieval) per latitude and longitude grid over given time period
Cloud-Sky ACA Frequency (Active)	CALIOP	(# of CALIOP observations with AOD > AOD baseline located above a cloud with COD > 0) / (# of CALIOP observations with COD > 0) per latitude and longitude grid box over given time period
All-Sky ACA Frequency (Active)	CALIOP	(# of CALIOP observations with AOD > AOD baseline located above a cloud with COD > 0) / (total # of CALIOP observations) per latitude and longitude grid box over given time period
Cloudy-Sky Frequency	MODIS	(# of observations with Cloud Fraction of unity (CF =1) / total # of MODIS observations)

Table 2. Global cloudy-sky relative frequency and data counts for the sensitivity test carried out in Sect. 5. Aerosol and cloud layers retrieved with 'intermediate' or 'strict' QA metrics are considered in this analysis. A total of five different threshold tests are applied to both day and nighttime CALIOP cloud and aerosol layer products.

	Day	Night
Total Cloudy Scenes (Column COD > 0 /0.3/2.5)	100,028,240/ 54,801,072/ 28,559,920	91,828,232/ 52,634,300/ 25,897,344
Data Counts / Mean Global ACA Relative Frequency		
COD > 0 & AOD > 0	1,193,048/ 1.79 %	3,368,351 / 4.5 %
COD > 0.3 & AOD > 0	789,652/ 2.0 %	2,795,442 / 6.1 %
COD > 2.5 & AOD > 0	556,097/ 2.5 %	2,091,310/ 8.09 %
COD > 0.3 & AOD > 0.015	597,917/ 1.63 %	1,516,547/ 3.54 %
COD > 2.5 & AOD > 0.015	420,778/ 2.0 %	1,167,569/ 4.52 %
COD> 0 & AOD > 0.015	904,892 / 1.46 %	1,765,620 / 2.6 %

Table 3 Seven and a half year above-cloud aerosol cloudy-sky frequency, ACAOD and clear-sky AOD inter-annual variability analysis for the selected target regions. Aerosol and cloud layers retrieved with 'intermediate' or 'strict' QA metrics are considered in this analysis. Yearly variation for the entire globe is also included. For each region, inter-annual variability (frequency change per year) for the three parameters, the ACA cloudy-sky frequency, ACAOD and clear-sky AOD values are reported. Note that the inter-annual variability for clear sky AODs is estimated using 100% cloud free data from the CALIOP cloud and aerosol layer products.

Region	Latitude (°)	Longitude (°)	Slope /per year (CALIOP day-time) (%)	Trend Significance CALIOP day-time ($\frac{\acute{\omega}}{\sigma_{\acute{\omega}}}$)	Slope /per year (CALIOP night-time) (%)	Trend Significance CALIOP night-time ($\frac{\acute{\omega}}{\sigma_{\acute{\omega}}}$)
ACA cloudy-sky frequency (%)/ Above-cloud aerosol AOD / clear-sky AOD						
Southern Africa	37°S - 5°N	30°W - 30°E	0.007/ -0.001/ -0.0004	0.009/ 0.18/ 0.04	0.148/ 0.0005/ 0.0009	0.159/ 0.067/ 0.08
Northern Africa	5°N - 35°N	70°W - 25°E	0.05/ -0.0006/ -0.001	0.116/ 0.035/ 0.07	0.07/ -0.0001/ -0.002	0.133/ 0.005/ 0.09
Southeast Asia	10°N - 25°N	90°E - 150°E	-0.04/ 0.004/ -0.002	0.080/ 0.17/ 0.1	-0.010/ -0.0012/ -0.0004	0.026/ 0.07/ 0.02
China	30°N - 55°N	110°E - 160°E	-0.084/ 0.0006/ 0.0009	0.238/ 0.090/ 0.05	-0.10/ -0.0006/ 0.0002	0.088/ 0.10/ 0.008
Middle East	10°N - 40°N	30°E - 55°E	0.36/ 0.004/ 0.006	0.239/ 0.15/ 0.16	0.339/ 0.004/ 0.005	0.238/ 0.09/ 0.13
South America	20°S - 10°N	105°W - 60°W	-0.078/ 0.0018/ -0.0016	0.189/ 0.18/ 0.12	-0.157/ -0.0002/ -0.0019	0.109/ 0.03/ 0.09
India	0° - 30°N	60°E - 85°E	0.10/ 0.001/ 0.0084	0.106/ 0.08/ 0.20	0.08/ -0.0035/ 0.010	0.110/ 0.064/ 0.19
North America	20°N - 60°N	160°W - 110°W	-0.05/ 0.0005/ 0.00002	0.082/ 0.06/ 0.003	-0.074/ -0.0005/ -0.0003	0.045/ 0.10/ 0.04
Southern Oceans	40°S - 12°S	35°E - 115°E	-0.04/ 0.0004/ 0.0012	0.120/ 0.083/ 0.29	0.05/ 0.0004/ 0.0008	0.037/ 0.078/ 0.21
Global			-0.004/ 0.0004/ 0.0006	0.049/ 0.16/ 0.13	-0.02/ 0.0004/ 0.0007	0.05/ 0.15/ 0.18